The Role of Fiber Bundle and Membrane Subunits in Aortic Valve Function

A Thesis

Submitted to the Faculty

of

Drexel University

by Christopher Allen Rock

in partial fulfillment of the

requirements for the degree

of

Doctor of Philosophy

July 2015

Dedications

To the Rock Family:

Many of us have found the calling to medicine; to help people's lives, ease their suffering, and helping them find fulfillment in what time they have in this life. I am proud to follow in this and dedicate myself to such a cause. I hope this work is one of many contributions I will be able to make. I especially want to dedicate this in loving memory to two members of the Rock family who are no longer with us.

To my late grandfather, George Rock:

On some level, you made me more acutely aware of the need of this work with how you left this world. However, more so you showed me to how to live a fulfilling life through hard work, dedication, and a bit of cleverness. I will do my best to carry on those ideas and your spirit.

To my late cousin, Shawn McNabb:

Your dedication to the calling of medicine went beyond all of us. I miss you dearly and hope you are at peace.

Acknowledgements

No true engineer's work is completely his own. This thesis is a product of the collaboration and help of many people who I would like to now acknowledge:

To my advisor, Dr. Todd Doehring, this thesis could not have begun without your guidance and support. I especially want to thank him for his help with the optical tracking algorithm and the non-linear viscoelastic direct fitting of the mesostructure biomechanical data which he invested much personal time in helping me produce results.

To my advisor, Dr. Lin Han, thank you for stepping up to help someone a bit outside your area of study get across the finish line. You have shown me a lot with what it takes to polish and refine work so it is presentable to both colleagues and the overall scientific community.

To my committee members: Dr. Shieh, Dr. Balasubramanian, Dr. Marcolongo, and Dr. Patel. I would like to thank you not just for your time and energies put to reviewing my work but also for challenging me and pushing me to develop beyond just someone with the technical and analytical skills.

To Dr. Oluseeni Komolafe, without your numerous hours of work, valuable consultation, and the innumerable other ways you helped me through this thesis, I would have struggled significantly more to reach completion.

To the Biomed staff at Drexel: Danielle Crocker, Natalia Broz, Frank Kepics, Lisa Williams, you each have done much to help me with whatever odds and ends I needed always being both capable and a pleasure to be around.

To the Drexel Machine shop, thank you for donating both materials and your expertise allowing me to build the testing system used in this thesis.

To the Biological Sciences Department at Drexel, thank you for allowing me to work for them during my time at Drexel. It was always one less thing I had to worry about knowing I was able to find work with you and accommodating me during my cancer.

To my parents, Tim and Karen Rock, thank you both for your continuous support during my journey here at Drexel. I know it took longer than we originally expected.

To my many friends who gave me multitudes of support, sounding boards for ideas, audiences for my presentations, and above all else believing that I would get this done, you all have my deepest thanks.

Table of Contents

List of Illustrations

List of Tables

Abstract

The Role of Fiber Bundle and Membrane Subunits in Aortic Valve Function

Christopher A Rock

Heart valves are complex arrangements of collagen fibers and membranes that oppose retrograde blood flow during contraction of the cardiac chambers. Through its amazing lifetime, the normal healthy valve cycles over *3 billion times.* However, disease (such as stenosis/calcification or mechanical wear) can cause the valve to malfunction, permitting backflow or failing to properly open. When a valve cannot be salvaged, treatment can require replacement of the valve to improve hydrodynamic behavior. Replacements are either a mechanical valve or, more commonly, a bioprosthetic valve made of either porcine valves or bovine pericardium. Although bioprosthetic implants are highly successful short-term, their long term durability is still limited. Alternatively, the patient can use a synthetic mechanical valve which will likely necessitate blood thinners for the remainder of his/her life. Thus, there is need for replacement valves that possess both superior durability and hemodynamic function. Current bioprosthetic and mechanical designs do not fully consider the underlying native fiber structure of the aortic valve, nor their fiber-scale biomechanical properties. In the past, the challenge of testing at the fiber bundle length scale precluded experimentation. Thus, there was little previously known regarding how the fiber bundles and membrane structures are arranged as well as their exact role in aortic valve function.

The overall objective of this work was to perform experimental and analytical analyses of the individual collagen fiber and membrane "mesostructures" of the aortic valve. We developed a novel experimental/analytical system to investigate these structures in detail. Using this system, we were able to perform a detailed characterization of the substructures' morphology and the first quantification of their biomechanical properties. This work offers new insights in structure-function adaptations of the native aortic valve at the tissue level. In addition to the application of a more effective replacement valve design, the results of this thesis can be used in the generation of more precise mathematical models of aortic valve loading behavior.

Chapter 1: Background

1.1 Aortic Valve Anatomy and Pathology

Heart valves are specialized structures that prevent the backflow of blood into the chambers of the heart. This function can be undermined by diseases such as calcification, lesions, or congenital defects [1]. In 2009, over 139,000 medical procedures were performed in the US related to heart valves, of which 89,000 were in patients 65+ years old [2]. This presents a growing concern considering the rising elderly population as heart valves tend to lose their ability to stretch with age [3]. Two-thirds of heart valve related hospital discharges and mortalities involve the aortic valve [2], hence the aortic valve is of particular interest. If conservative treatment such as valve repair cannot sufficiently restore a valve's function, a replacement valve made of either synthetic or biological material will be installed [4]. While the current prosthetic valves have undeniable medical value, there are drawbacks in terms of durability and biocompatibility which underscore the need for better understanding of valve 'mesostructure' (i.e. fiber bundle and membrane structures) to potentially enable a more modern tissue engineered repair/solution [5, 6].

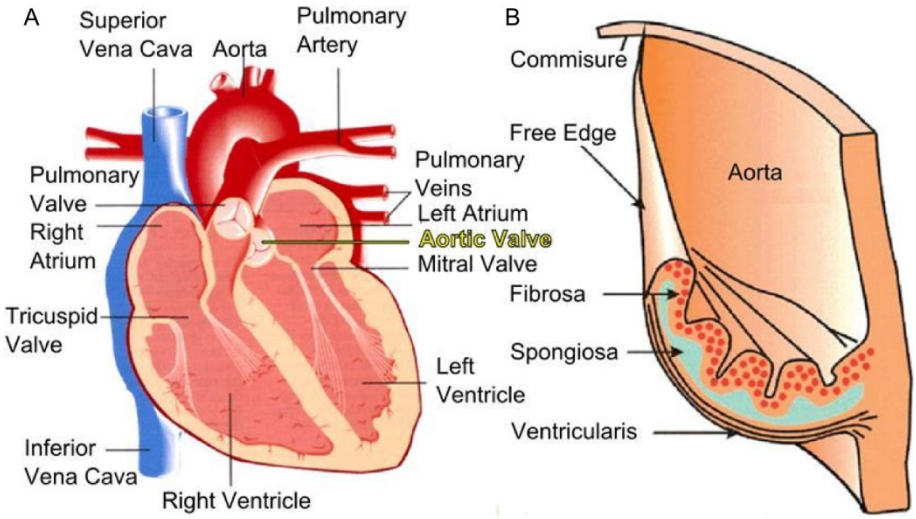

Figure 1 (A) Illustrations of cross-section of the heart showing valves (B) Layers of the aortic heart valve (Source: M. K. Todd C. Doehring 2005)

The aortic valve is an arrangement of 3 leaflets identified by the presence of 2 coronary artery ostioles yielding a left coronary, a right coronary, and a non-coronary leaflet (Figure 1A). Current anatomic texts simply describe the

leaflet as comprised of three layers (Figure 1B) [7]. On the aortic side, the fibrosa is an arrangement of collagen sheets and large collagen fiber bundles. The ventricularis is a dense array of collagen and elastin on the ventricular side of the valve. Between these outer layers is the spongiosa, a layer rich in proteoglycans. Studies suggest the spongiosa facilitates the fibrosa and ventricularis sliding along one another as a lubricant[8]. The layered structure (taken largely from inspection and analysis of histological specimens) is described as an adaptation to the multiple functional requirements for frequent flexion duty cycle, durability, high shear compliance, and high pressures of aortic hemodynamics [8-10]. This idealized description is useful as a basic representation of valve anatomy. However, it is well known that valve material and biomechanical properties can vary from leaflet to leaflet and even within an individual leaflet [11-13].

Figure 2 Illustrations of (A) a normal aortic valve, and (B) a stenotic valve. The normal valve has collagen fibers/membrane structures organized for optimal function. The stenotic valve is disorganized with local regions of calcification, severely compromising function. The stenotic valve will likely have to be replaced.

1.2 Treatment Strategies and the Need for a Tissue-Engineered Solution

When a valve cannot be repaired such as the valve in Figure 2, it is replaced with either a mechanical valve, a valve derived from animal material, or a valve created from synthetic polymers. The porcine valves are popular bioprosthetic replacements given the similarity between pig hearts and human hearts [14]. Currently, the expected functional life of a porcine aortic replacement valve is 12 years [15] and 15 years for a bioprosthetic derived from bovine pericardium [16]. Frequently, when these bioprosthetic valves fail it is due to either tears in the leaflets or damage in the tissue leading to calcifications which in turn impede valve function [17]. Mechanical valves are

significantly more durable with an expected life of over 25 years [18]. However, they required the patient take blood thinners and sometimes have audible clicks which reduces patient quality of life. At present, no replacement valves can fully restore the flow dynamics of the native, healthy valve. This motivates refining the designs for replacement valves with the long goal of developing a tissue-engineered prosthetic valve.

1.3 Tissue Engineering Strategies

Decellularization has potential for producing bioprosthetic replacement tissue. By removing the cellular factors, the material should produce less of an immune response in the patient [19]. It is then a matter of how much the mechanical properties are affected [20]. Jun Liao from the University of Pittsburg tested how an anionic detergent (SDS), enzymatic agent (Trypsin), and a non-ionic detergent (Triton X-100) altered the stiffness of porcine aortic valve leaflets. The result is a significantly less rigid tissue when each agent is applied (Figure 3). This calls to question the durability of any replacement created using these techniques [21]. As other researchers have found conflicting results regarding the integrity of decellularized valves, this remains a point of contention in the field [22].

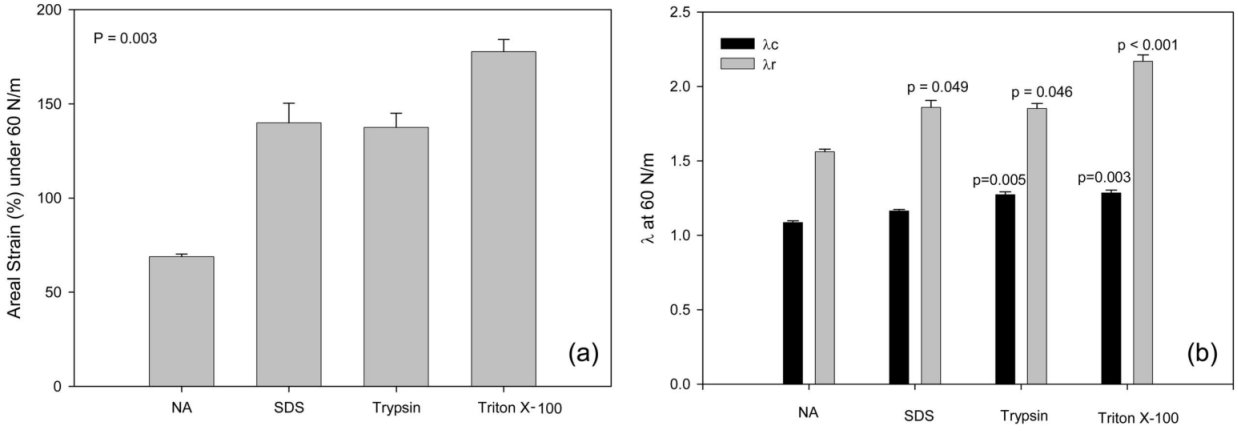

Figure 3 Aortic valve extensibility at 60 N/m tension for (a) areal strain and (b) peak stretch ratios. All decellularization protocols increased the extensibility (Source: Liao et al 2008).

An alternate strategy has been seeding cells into non-biologically derived scaffold produces by such techniques as electrospinning [23-25]. This has the advantage of directly controlling the mechanical properties of the substrate. The techniques behind such designs are continuing to develop such as fiber reinforced scaffolds to distribute loading

more uniformly [26]. However, all current designs still needing further refinement to be ready for implantation in humans [27].

In developing a tissue engineered replacement, a thorough understanding of the native tissue's biomechanical properties is essential. This is accomplished through biomechanical testing and the development of accurate structure-based models. The models will both serve as a benchmark for the physical requirements as well as provide insights as to how the native valve has adapted for hemodynamic and biomechanical function [28].

1.4 Biomechanical Testing and Analysis of Aortic Valve Properties

The study of heart valve leaflets was initiated in the 1930's by Louis Gross and M.A. Kugel of Mount Sinai Hospital. They dissected and plated out specimens from 1000 human hearts giving one of the first comprehensive exploration of the tissue. It was this work which identified and first described the various layers of the human heart valve [10].

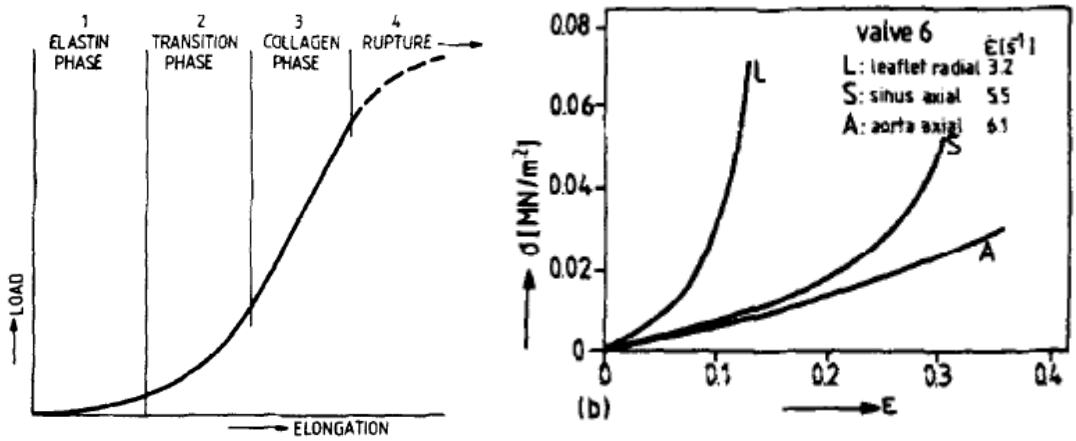

Figure 4 (a) Load-elongation curve typical for soft tissue uniaxial tests. There are 4 different loading phases where the strain is composed. (b) Stress-strain data for different parts of a valve at different scaling factors. (Source: Sauren 1983)

The first uniaxial strain tests on aortic valve specimens were done in 1973 and largely explored the non-linear elastic properties of the tissue [29]. This encouraged additional study by Sauren et al to quantify the relaxation of the

viscoelastic material. Their estimate of the stress-strain data of various regions of the heart valve are in Figure 4 [30].

1.4.1 Regional, Layer, and Leaflet Variability

Dr. K. Jane Grande et al published one of the first studies that identified the variability in peak stress and peak strain through the regions of a leaflet and between the three leaflets in human aortic valves. They observed that within a leaflet: stress is highest at the belly and free edge and lowest at the attachment edge while strain is also highest at the belly and lowest at the attachment edge. Across the leaflets: the non-coronary has the highest stress while the left coronary has the lowest stress. Additionally, strain is highest in the right coronary leaflet and lowest in the left coronary leaflet [31].

Dr. Ivan Vesely directly compared the ventricularis and fibrosa layers extensibility (strain to high-modulus phase) and elastic modulus in both the circumferential and radial directions [32]. The test protocol microdissected the leaflets from porcine aortic valves to sever the fibers connecting the layers. The specimens consisted of strips from the center of each layer clamped into an INSTRON tensile testing device. The resulting tests found significant higher stiffness in the circumferential direction for both the fibrosa (13.02 kPa vs 4.56 kPa) and the ventricularis (7.41 kPa vs 3.68 kPa). These trends were attributed to the increased alignment of collagen in the circumferential direction. With regards to extensibility, the fibrosa had no significant difference in the radial and circumferential directions (27.8% strain) while the ventricularis was more extensible radially (62.7% vs 21.8% strain) [32]. The limited extensibility of the fibrosa was surprising given previous studies had found the intact layers could extend approximately 60% radially [33, 34]. The discrepancy was attributed to the folding of the fibrosa layer in its intact state which would be smoothed out in the extensibility tests into a flat sheet of collagen. Based on the visual crimping patterns, a relaxed leaflet has the fibrosa in compression and the ventricularis in tension [32].

Perhaps the most cited work on heart valve mechanics was done by Dr. Michael S. Sacks' lab at the University of Pittsburgh. He and his colleagues performed bi-axial testing which evaluated the mechanical properties of the three layers of the leaflet [35] and developed a layer based model [8]. They found the fibrosa tends to be the major load bearing layer (Figure 5). The leaflets show a complicated anisotropic mechanical behavior distinct in the radial and circumferential directions [36].

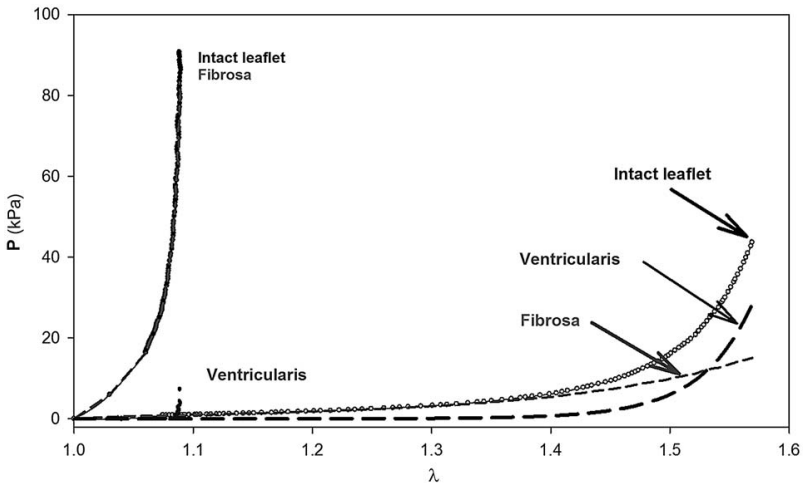

Figure 5 Stress-stretch data from biaxial loading experiments under physiological strains of intact leaflets and the individual layers separated out. The ventricularis's loading curve seems to most closely follow that of the intact leaflet (Source: Michael S. Sacks 2009).

Dr. Balguid et al examined how the individual collagen fibrils vary in terms of their density and diameter across the regions of the human aortic valve leaflets using transmission electron microscopy. The density of the fibrils negatively correlated the fibril density. The commissure's fibrils had the greatest diameter and lowest density. The belly had intermediate fibril diameter and density. The fixed edge had the highest density of fibrils of the smallest diameter. Thus, the greater fibril diameter occurred in the regions with the greater stress. The suggestion is that larger diameter collagen fibrils have greater capacity for cross-linking and thus can carry greater loads. These results demonstrate that the stress adaptations of the aortic leaflet operate at the fibril-level of organization [11].

1.4.2 Time-Dependent

The time-dependent or viscoelastic biomechanical studies focus on two behaviors common to soft tissues: creep and relaxation. Creep is an increase in stretch of a material that is held at a constant stress. Relaxation is the decrease in stress of a specimen held at a constant strain. The goal of the work is to both quantify these behaviors as well as offer a mechanism for their occurrence. Current theories are that the viscoelasticity may be either an innate property of the collagen fibrils or a product of fibril-fibril interactions [37].

Dr. Vesely's 1992 study examined the relaxation rates for the fibrosa and ventricularis layers in the radial and circumferential directions. Overall, there was a faster relaxation in the radial direction with this disparity being more pronounced in the fibrosa layer. He suggested that the increased alignment of the fibrosa in the circumferential direction reduced its capacity to migrate and realign which would facilitate relaxation [32].

A 2007 study by John Stella, Jun Liao, and Michael Sacks explored aortic valve creep and relaxation with regards to direction (radial vs circumferential) and strain rate (from 1.2%/s to 381%/s) at physiological loading. The observed relaxation in stress was significantly greater in the radial direction relative to the circumferential direction (33.28% vs 27.51%). The directional relaxation variability was attributed to the anisotropy of the leaflet's collagen fibril arrangement. The collagen would have to rotate more for radial loading which would alter the interactions between the fibrils. The creep was negligible in either direction regardless of loading rate. They inferred from the lack of observed creep that the mechanics of creep and relaxation are independent in aortic valve tissue. Overall, the strain rate had no significant effect on the viscoelastic properties [37].

Sample	Strain Rate (%/min)	UTS (MPa)	Failure Strain (%)
Circumferential	6	3.44 ± 0.57	45.07 ± 1.25
	60	3.68 ± 0.12	31.54 ± 1.69
	600	4.45 ± 0.13	27.56 ± 1.96
Radial	6	0.34 ± 0.03	87.6 ± 1.78
	60	0.50 ± 0.03	77.15 ± 0.03
	600	0.84 ± 0.05	61.11 ± 0.63

Table 1 Values (mean ± SD) of ultimate tensile strain (UTS) and failure strain at different strain rates and in both directions (Source: Anssaari-Benam PhD thesis 2012)

The most current comprehensive study on the viscoelastic properties of the aortic valve was done by Dr. Anssaari-Benam in his PhD thesis at the University of London. His thesis evaluated the viscoelastic and failure

properties of the aortic valve as a function of directionality, loading rate, and strain [38]. The failure strain was significantly higher in the radial direction and consistently decreased with strain rate as shown in Table 1. The relaxation behavior had values consistent with those reported by Stella et al at moderate strains (~10% failure strain). However, as the strain levels increased, the degree of relaxation reduced. This is summarized in Table 2. He suggested that there is a single mechanism behind the relaxation at low strains (<5% failure strain) and two mechanisms present at high strains (>5% failure strain). The critical difference being at higher strains the collagen crimp has been mostly eliminated. The first mechanism was proposed to be a structural influence of the glycoaminoglycans. The second mechanism would be an interaction between the collagen fibrils such as slippage. The creep behavior had a small increase with greater strains in the both directions with consistently greater creep in the radial direction [38]. There have been limited proposed mechanisms for creep in heart valve tissue as it is relatively small at physiological loading.

Stress-relaxation				
	Specimen			
	Circumferential		Radial	
Strain Increments ($\%\varepsilon_{failure}$)	Relaxation Modes*	Relaxation at 300s (%)	Relaxation Modes*	Relaxation at 300s (%)
3	S	95.80 ± 2.91	S	85.09 ± 3.45
5	S	41.25 ± 3.56	S	76.96 ± 2.13
10	D	34.75 ± 2.04	---	---
15	D	29.72 ± 1.40	S	41.20 ± 1.44
20	D	26.35 ± 1.78	S	38.49 ± 2.13
30	D	22.80 ± 2.86	S	34.08 ± 2.22
40	---	---	S	30.01 ± 2.01
50	D	19.81 ± 1.28	S	26.59 ± 1.82
60	D	18.22 ± 1.71	---	---
80	D	16.38 ± 1.82	S	21.48 ± 2.80
90	---	---	S	18.85 ± 2.27

Table 2 Total stress-relaxation (mean ± SD) for different strain increments in the radial and circumferential directions (Source: Anssaari-Benam PhD thesis 2012).

1.4.3 The Role of Elastin

As the dry weight of the aortic valve leaflets is 50% collagen and 13% elastin, much of the emphasis in the research has been on the biomechanical role of collagen as the relative compositions suggested the contribution of elastin is minimal [39]. However, the leaflets are capable of strains greater than 50% with elastic recoil, a behavior that cannot be fully accounted for by collagen alone. Thus, there is likely a significant influence by elastin on the leaflet's biomechanical properties [40]. Dr. Ivan Vesely directly assessed this by measuring the mechanical properties of aortic valve leaflet specimens and then retesting them after chemically digesting everything other than the elastin [41]. The elastin showed two major forms: amorphous, continuous sheets in the ventricularis and discreet fibrils either loose or arranged into a mesh in the fibrosa [40]. The isolated elastin was highly extensible (>>100% strain) with a stiffness $1/1700^{th}$ of the intact leaflet and a very linear tension-strain curve. The elastin was significantly more present in the ventricularis compared to the fibrosa with an order of magnitude higher mean fracture tension. Thus, the contribution of elastin to the fibrosa is minimal but it plays a significant role in the ventricularis's biomechanics especially in the radial direction. The elastin fibers shrank 10-30% following the removal of collagen demonstrating that they were coupled and under tension with the collagen fibrils. At low strains (<0.15), the fibrosa is folded or under compression so the ventricularis contributes the majority of the tension. As the strain increases, more of the tension is carried by the fibrosa with it gradually locking in place as the collagen becomes more aligned. The ventricularis in turn, serves to help restore the leaflet into its relaxed state with the folded fibrosa which requires the highly distensible elastin [41]. These concepts has been applied by Dr. Vesely's lab to develop a bioreactor to produce sheets of elastic coupled with collagen fiber bundles [42].

A follow-up study by Tseng and Grand-Allen at Rice University examined the role and morphology of elastin in the spongiosa using immunohistochemistry as well as scanning electron microscopy. All regions of the leaflet had a consistent form of the elastin in the spongiosa and that was of a "finely fibrous, interwoven, porous network which extended from the ventricularis to the fibrosa." The spongiosa layer containing elastin was thickest in the hinge and coapting region while being thinnest in the belly of the leaflet. The elastin in the hinge and coapting region had a rectilinear pattern. They suggested that the additional thickness as well as the organizational pattern aides the flexing of the leaflet by allowing the fibrosa to buckle rather than undergo compression. This could also assist in absorbing the reverse blood pressure during diastole. The thinner spongiosa in the belly would limit the relative movement and

shear between the ventricularis and the fibrosa layers. Thus, they suggested the elastin here serves to connect the layers and aid in the restoring of the original conformation. Their study observed no significant differences between the three leaflets nor circumferentially across the leaflet. [43].

1.5 Computational Modeling of Valves

Computational models allow for rapid simulation to evaluate prospective designs and thus the development of computational models is critical to the field of heart valve prostheses [44]. Current models tend to represent the structure of the leaflet as a finite element (FE) mesh [45]. Unfortunately, the complexities of the bending movements of the heart valve are often overlooked in two dimensional models [46]. The current efforts are to establish a model that is representative of the heart valve's mechanical properties at the organ, tissue and cell levels [44].

One of the earliest finite element models of the aortic heart valve was published by Phillip Gould, Altay Cataloglu and Richard E Clark in 1976. The leaflets were represented with thin, curved triangular shell elements as shown in Figure 6. The data used in the model was derived from moulds of the human aortic valves created using low viscosity silicone rubber. They assessed 3 different geometric representations for the leaflet: an elliptical paraboloid, a paraboloid of revolution, and a spherical surface. This model acknowledged how the geometry of the leaflets influenced the stress and strain fields [47, 48].

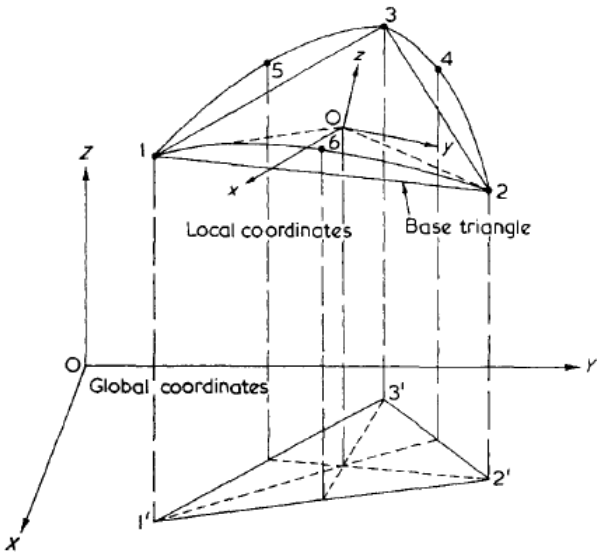

Figure 6 Geometry of finite element model used by Gould et al. in 1976

J. Li, X.Y Luo, and Z.B. Kuang published a nonlinear anisotropic model of the porcine aortic heart valve. This model represented the collagen and elastin of the valve leaflet as a fiber-reinforced composite material [49].

Hadi Mohammadi, Fereshten Bahramian, and Wankei Wan developed a high order finite element model of heart valve leaflet tissue as shown in Figure 7A. The constitutive element had bidirectional mechanical properties for the circumferential and radial directions (see Figure 7B). Their goal is to bring the field closer to being capable of mesh-free models of the heart valve tissue [46].

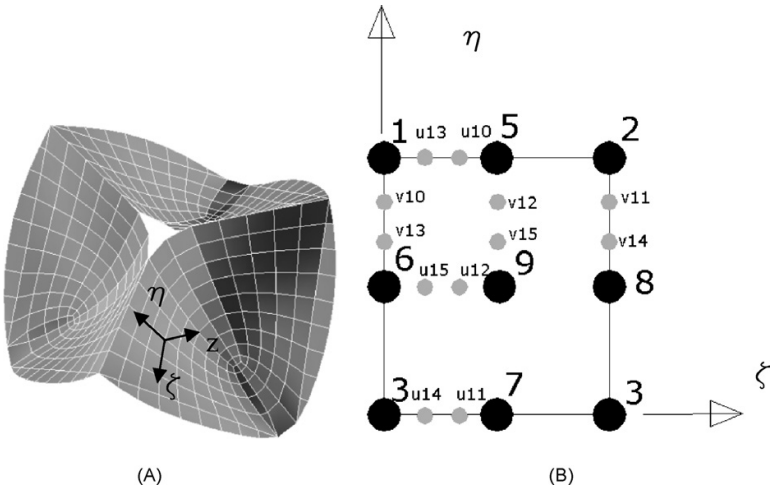

Figure 7 (A) A model of the heart valve tissue using 183 high-order elements. (B) A single high-order with major and minor nodes. (Source: Mohammadi et al. 2009)

In 2010, Weinberg et al published that the behavior of the overall heart valve in healthy and disease state cannot sufficiently be described solely at the individual length scales of organ, tissue, cell, or molecule. Thus, their efforts have been to produce a multiscale model approach. The final results are still forthcoming [28].

Carmody et al had developed a full finite element model of the left ventricle to represent blood flow through the aortic valve [50]. They used a simplified shell to represent the aortic valve leaflets as a non-linear elastic material that was previously developed by Black et al in a study of bioprosthetic heart valves [51]. The goal was to represent the fluid-structure interaction through the cardiac cycle. This was able to give spatial and temporal data showing the

loading conditions of the valve during opening and closing. A limitation of this approach was it used three symmetric leaflets [50].

Marom et al directly traced the major fiber bundles of the aortic valve to develop a structure-based model of the leaflets. They used the known mechanical properties of collagen and elastin for the biomechanical properties of the leaflets' fiber bundles and regions between the bundles, respectively. This model was compared to a another model of valve comprised of regular fiber bundle arrangements across all three leaflets. Their study found that by having an asymmetric arrangement of fiber bundles in the leaflets, the valve would open more rapidly with a larger opening area causing a greater peak flow. Additionally, in their model the leaflet with the least fiber bundles would open the most rapidly and undergo the greatest deformation which may be a root cause of damage in that region of the leaflet [52].

One of the more recent published models was created by Peter Hammer, Michael Sacks, Pedro del Nido, and Robert Howe RD. Their mass-spring representation of heart valve tissue was presented as an alternative to finite element models. This has masses at the vertices of the mesh connected by springs (Figure 8). The advantage of this model is in its computational time as speed limitations of finite element models prevent their application in patient surgery planning. The resulting model proved faster but less accurate than a simple finite element model in modeling the loading cycle of the heart valve[53].

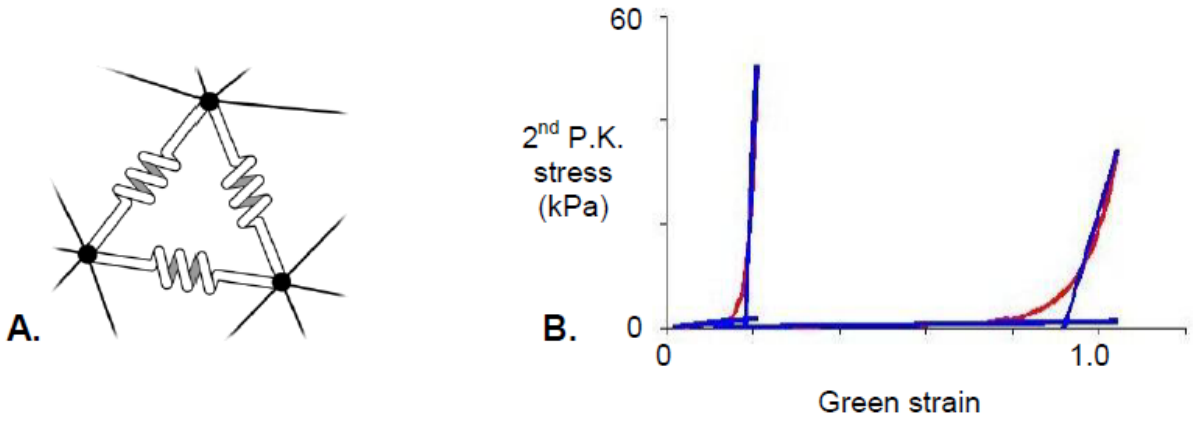

Figure 8 Components of the mass-spring model. (A) Vertices of the mesh are the locations of the mass and edges of the triangles of the mesh are springs. (B) The spring constants are approximated with a bi-linear relationship. (Source: Hammer et al 2011)

1.5.1 Modeling non-linear elastic, viscoelastic materials

Collagen fibers display a time evolving component of their stress-strain relationship making them a viscoelastic material. Most notable among viscoelastic behaviors are creep, an increase in material strain when held at a constant stress, and relaxation, a decrease in material stress at constant strain [54]. Also, soft tissue specimens typically have a non-linear transitional phase in their stress-strain curve after which the curve becomes more linear [55] as shown in Figure 9.

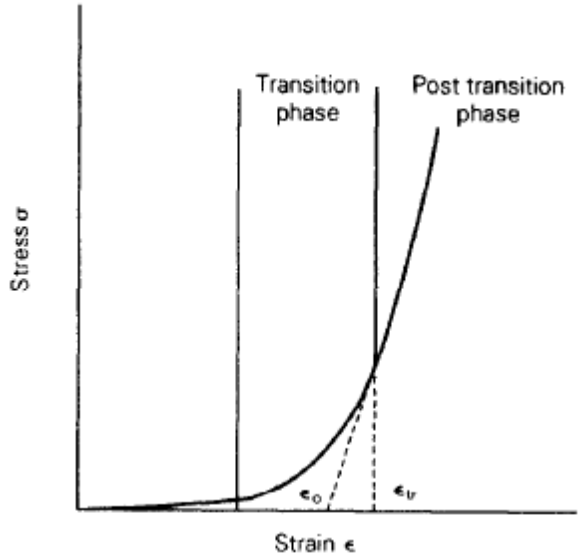

Figure 9: Stress-strain curve of a typical soft tissue showing pre and post transition phases. (Source: Mavrilas 1991)

The prevailing mathematical model for collagen and many other soft biological tissues mechanics is the quasi-linear viscoelastic (QLV) theory developed by Y.C. Fung. The QLV theory says that the stress-strain behavior of soft tissues can be separated into elastic and time dependent behaviors. Thus, the QLV equations represent the mechanics of the material using a non-linear elastic stress-strain relationship with a reduced relaxation equation. The non-linear elastic behavior quantifies the curve of the stress-strain data during loading as an exponential. The reduced relaxation equation is composed a dimensionless constant and two time constants of the relaxation curve from the experimental data[56]. There may be difficulty matching the heart valve tissue biomechanics to a traditional QLV model. Two alternative mathematical adaptations have been reviewed that have been applied to collagen fibers by Dr. Doehring at Drexel [57] and Dr**.** Ali Nekouzadeh at Washington University in St. Louis [58]**.**

1.6 Heart Valve Mesostructure

Anatomically, the valves have been described as a 3-layered structure (Figure 1B) with a fibrosa layer on the aortic side that contains large collagen fibers, a ventricularis on the ventricle side that is composed mostly of elastic, and an intermediary spongiosa layer that is high in proteoglycans. Recent studies, however, have shown that the aortic valve is a much more complex structure that defies the simplistic 3-layer description[59]. The leaflets of the valves are composed of multiple collagen fiber bundle branches, sub-branches and membranes as shown in Figure 10. These fiber bundles are suggest to help transmit the load of the leaflets to the aortic root [7]. The arrangement of tissue at a scale between the organ and microscopic levels is referred to as the *mesostructure*[59]. Generally, the collagen fibers are oriented to run circumferential to the leaflet [60] which accounts for the increased stiffness in that direction[55]. The elastin fibers tend to run radially [60]. However, previous studies tended to not delineate between collagen fibrils collected in bundles and ones embedded in the fibrosa and ventricularis. There is significant difference in the bundle diameters and fiber bundle counts between the three leaflets of the aortic valve as well as their respective cusp areas. This asymmetry is likely a hemodynamic adaptation. The multiple layers of membrane run between the fiber bundles are very thin and comprised of collagen that is variably aligned. It is this arrangement of branches, sub-branches, and membranes which give the valve leaflets the tensile strength required while maintaining high flexibility for the opening phase of the heart cycle [59]. The mechanics of the valve are dependent on these fibers realigning, sliding, pulling on the underlying membrane and performing other non-affine deformations which requires a sophisticated model to represent [36]. Figure 10 shows the optical property of collagen known as birefringence that we take advantage of in our imaging and testing methods. A birefringent material has at least two different indexes of refraction for different orientations of transmitted light. By using light polarized to a particular orientation, optical information can be gathered from a material that would normally be translucent.

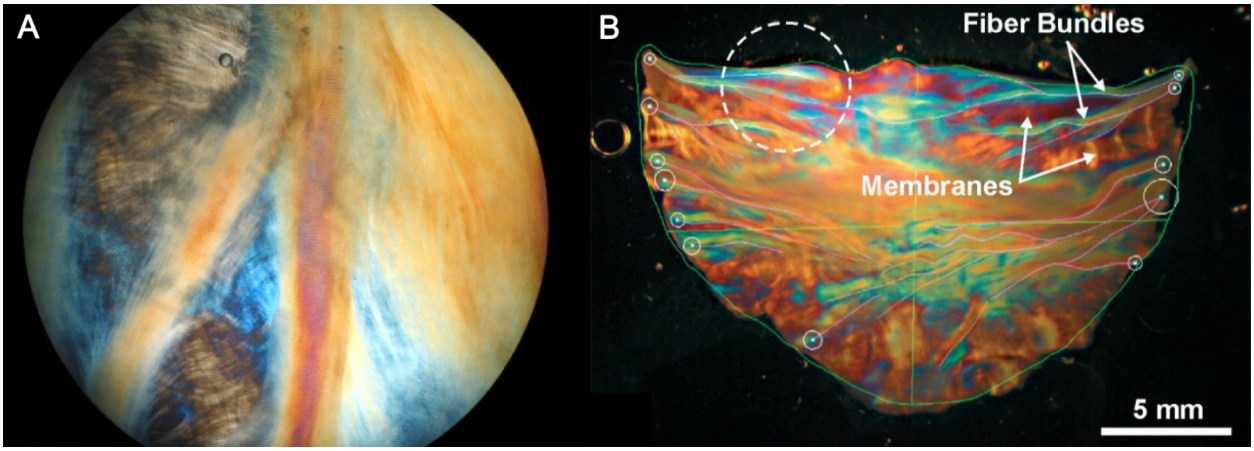

Figure 10 Polarized light images of aortic heart valve: (A) Close up showing distinct membrane and fiber structures. (B) Full right coronary leaflet. (Source: M. K. Todd C. Doehring 2005)

There have been some models presenting the leaflet tissue as a composite of membrane and fiber structures [28]. However, the data used to generate those models is derived from mechanical tests of the fiber bundles and membranes combined. The mechanical properties of the individual mesostructure elements have yet to be comprehensively documented due to the difficulty with testing at that scale [59]. That is the gap in the knowledge of the field this thesis will address. While the effects of individual fibers may "average out" in thicker soft tissue specimens[61], the individual collagen fiber bundles play a key role in the function of the aortic heart valve. This information will expand our knowledge of the tissue's behavior in tension which can be incorporated into a more accurate model of the entire heart valve leaflet.

Overall Objective, Specific Aims, and Hypotheses

Our overall objective for this thesis is: **To understand the roles of fiber bundle and membrane substructures in aortic valve function through morphological and biomechanical evaluation.**

To that end, we proposed the following three specific aims:

Specific Aim 1: To understand the morphological organization of aortic valve fiber bundles.

Chapter 2 describes the work toward this aim. To accomplish this aim, we tested the following hypotheses:

H1: Fiber bundle organization varies between leaflets

H2: Fiber bundle organization varies between regions and sides of a leaflet

Specific Aim 2: To develop a system for mesostructural biomechanical testing.

This aim is explored in Chapter 3 and as it is a technical aim, there is no hypothesis.

Specific Aim 3: To analyze the non-linear elastic and viscoelastic properties of aortic valve's mesostructure.

Chapter 4 describes the work toward this aim. To accomplish this aim, we tested the following hypotheses:

H1: Fiber bundle and membrane substructures have different elastic and viscoelastic properties

H2: Fiber bundle and membrane substructures' biomechanical properties vary between leaflets

Chapter 2: Analysis of Aortic Valve Fiber Bundle Organization

2.1 Introduction

Few studies have visualized and quantified the true fiber/membrane anatomical morphology at whole-leaflet scales [59]. The organization of larger leaflet fiber/membrane structures; existing on a scale between the macroscopic whole leaflet and the microscopic individual collagen fibers is referred to by us as the valve "mesostructure". Initial works exploring the aortic valve mesostructure has suggested that the aortic leaflet mechanical properties are related to conformation. For example, the asymmetric arrangements of fiber bundles in the left coronary leaflet may be related to optimization of blood flow and contribute its anisometric mechanics [31, 59]. Previous work using the polarized light microscopy highlighted some key differences between three leaflets, including their width, height and fiber bundle count. However, due to the imaging system limitations of spatial resolution [59], there was no detailed, mesoscale quantification of the leaflet structures, including the fiber bundle arrangements, membrane layout and the fiber-membrane anchoring. Knowledge of the mesostructural features, e.g., the fiber/membrane morphology, is critical for understanding the hierarchical design and function of the leaflets that can be used for biomedical applications such as prosthetic design.

The overall objective of this work in this chapter was to understand the key features of the whole porcine aortic valve leaflets at the sub-micrometer mesoscale using a custom-built autofocusing microscope with elliptically-polarized light capability. Due to the extreme difficulty in obtaining normal, disease-free human heart valves and the similarity between porcine and human valves [14], we used porcine whole leaflets as the model system. In this study, we quantified and compared sub-micrometer scale structure of the fiber bundles and membranes across the 3 leaflets, and between the left and right "sides" of each leaflet. We identified new features of the fiber bundles and their branching patterns that were not observed previously. Both qualitative and quantitative analyses were carried out to understand the heterogeneity at both the whole-organ scales between the three leaflets and at the mesoscale, fiber-bundle levels. The long term application of this study is to improve understanding of the complex structural basis for the valve's evolved biomechanical properties. The knowledge obtained from this study can be applied to models that more accurately depict valve dynamics and may guide the development of more anatomically accurate tissue engineered heart valves.

2.2 Materials and Methods

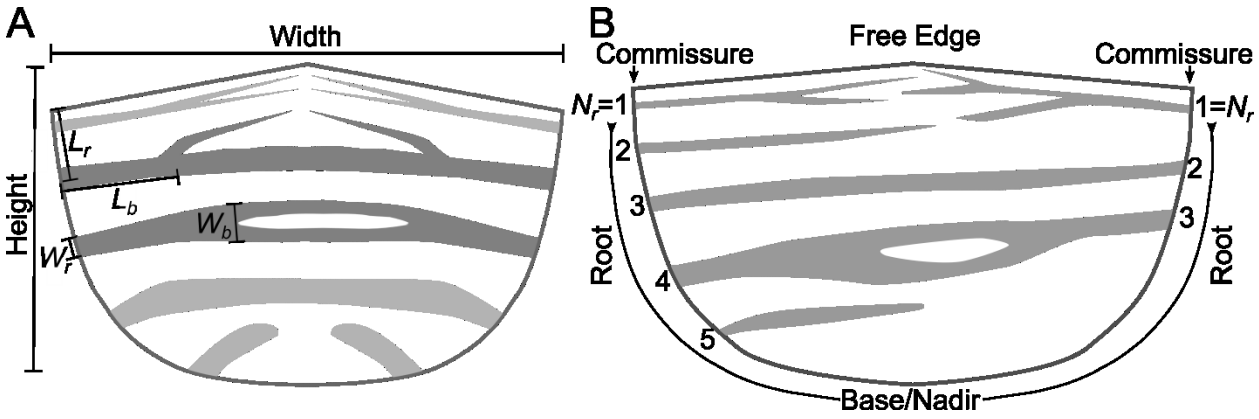

Figure 11 Schematics of a leaflet illustrating the structural parameters used to quantitatively describe the leaflet mesostructure, including: the length from the free edge along the root, L_r, the distance along a fiber bundle to the first branching, L_b, the width of the fiber bundle at the root, W_r, the width of the fiber bundle before the first branching, W_b, and the position of the fiber bundle from the free edge along the root, N_r.

2.2.1 Specimen Preparation

Fresh hearts from six month old pigs were acquired from a local abattoir and kept in ice during transport. The aortic valve was dissected out along with the aortic root from the heart. Each valve was cut through the root between the leaflets opening the valve to expose the leaflets. The three individual leaflets (left, non-coronary, and right) were carefully separated from the root using surgical scissors. The width of each leaflet was measured using a caliper in phosphate buffered saline (PBS) as the distance from left to right commissures (Figure 11A). The height of each leaflet was measured as the distance from apex of the free edge to base of the leaflet) (Figure 11A). All of the leaflets were used within 2 hours of extraction.

2.2.2 Imaging Procedure

Images were acquired using a digital camera (model PL-A686 PixeLINK Inc, http://www.pixelink.com) mounted to an Olympus microscope (model BX50 Olympus Inc.) equipped with polarizing filters and a ¼λ wave plate. The microscope was retrofitted with motors for fully automated stage control via a connected PC computer and custom software/hardware developed in-house. Leaflets were placed on a glass slide with the aortic side (fibrosa

layer) on top. We scanned leaflets from one heart with each layer on top and this produced negligible differences in the resulting images (Appendix Figure 35). In order to expose more of the structure to the camera and prevent the specimen from drying during image acquisition, a second glass slide was placed on top of the leaflet with additional PBS added to retain the hydration and reduce the formation of air. This second slide provided a slight pressure to flatten the leaflet. At 4× magnification, the camera field of view was 2.59 mm × 1.90 mm at a resolution of 1160 pixels/mm (0.862 μm/pixel).

During imaging, each leaflet was scanned left to right, row by row using an automated stage. Each image was focused using a novel algorithm that automatically adjusted for the best whole-image focus via a stepper-motor controlled z-axis. The autofocusing algorithm used edge detection and pixel counting to determine maximum sharpness (minimizing blur). The row-by-row scan produced a rectangular mosaic of images with 10% vertical and horizontal overlap between adjacent images. An elliptical light polarization was applied during imaging by rotating the polarizing filter 12° clockwise from a black background. Because collagen, the major protein of the aortic valve leaflet, is birefringent, polarized light produced color contrast on this translucent tissue as a result of collagen orientation changes induced light phase shifts [62]. We were thus able to delineate the collagen orientation and thickness without employing stains or markers from the resulted images with a dark violet background, a blue-green membrane, and red-yellow fiber bundles. These images were acquired via a custom designed/programmed GUI.

2.2.3 Quantification of aortic leaflet mesostructure

The image arrays were imported into the free Microsoft Image Composite Editor (ICE, Microsoft Inc.) for stitching using the planar scan modality. Accuracy of mosaic reconstruction was confirmed by visual inspection. The resulting composite images have a resolution on the order of 30,000 × 15,000 pixels.

Images of a total of twenty-five full leaflets were produced, including 8 left coronary, 8 non-coronary, and 9 right coronary leaflets. The image resolution was reduced by 2× before importing the images into GNU Image Manipulation Program (GIMP, http://www.gimp.org/) for visual inspection, general observations, and to calculate metrics of the fiber bundles. Decimation by 2 did not affect following measurements or statistics, and greatly reduced computer memory requirements and analysis time.

A list of quantitative parameters were measured to quantify the mesostructure of each fiber bundle using on-screen analysis tools via GIMP, as illustrated in Figure 11. These parameters include 1) the distance from the root origin of the fiber bundle to the free edge of the leaflet, L_r, 2) the distance from the root origin of the fiber bundle to the first major branching, L_b, 3) the width of the fiber bundle at the root, W_r, 4) the width of the fiber bundle before the first major branching, W_b, and 5) the fiber bundles' position from the free edge along the root, N_r. Data were imported into the R software (http://www.r-project.org/) and Matlab (Matlab2010a, The Mathworks, Inc., Natick, Massachusetts) for statistical analysis.

2.2.4 Statistical Analysis

To investigate the structural variations between these leaflets, we used analysis of variance (ANOVA) tests to compare the parameters from each leaflet. One-way ANOVA was used to compare leaflet height and width across the 3 leaflets and ratio of left versus right fiber bundle counts between each leaflet. We also used one-way ANOVA to study the effects of N_r, side of leaflet (left or right), and leaflet (left coronary, right coronary, or non-coronary) on W_r, L_b and W_b/W_r. Least squares linear regression was used to test the correlations between: N_r and L_r, L_b and W_r, W_b and W_r. Also, a Pearson's correlation coefficient, R, and probability of no correlation, *p-null*, were calculated between the sum of the widths of the leaflets of a valve and N_r, L_r, L_b, W_b and W_r. In all the statistical tests, a p-value of less than 0.05 was taken as statistically significant.

2.3 Results

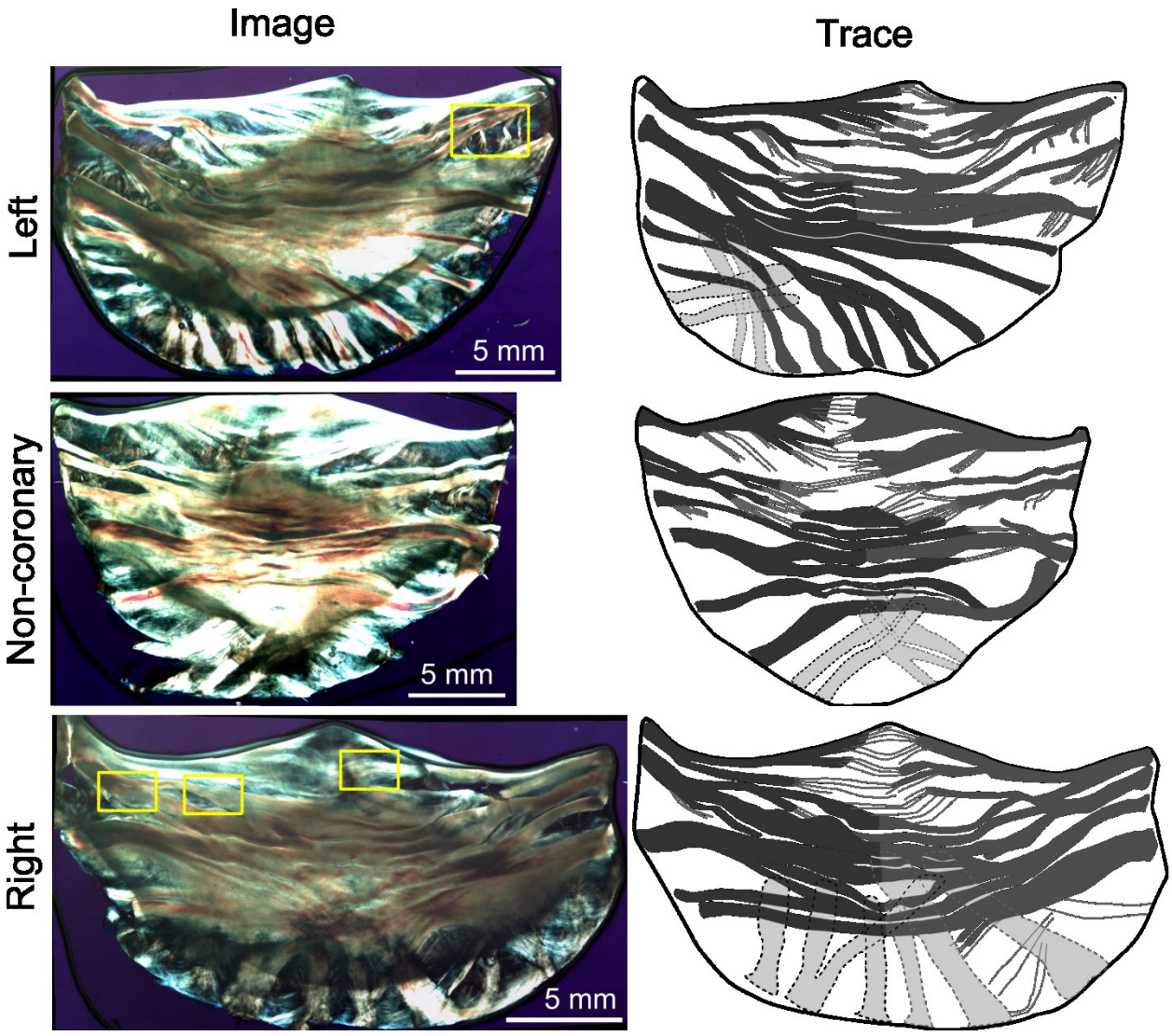

Figure 12 Polarized light images of three representative aortic valve leaflets. Images of three representative leaflets (left) along with traces of the major fiber bundles (right) to clarify primary structures of the leaflets. Fiber bundles appear yellow-orange and membranes appear blue as a result of the use of transmitted elliptically polarized light imaging. Clear differences in the fiber bundle arrangement were shown in the three leaflets. The left leaflet was the most asymmetric, while the non-coronary and right leaflets were more symmetric. Fiber bundles were most distinct at the edge (root) and branched or spread out towards the belly of the leaflet. Overall, fiber bundles appeared to present a cross-hatched, overlapping structure with thin connecting membranes. The yellow boxes identify the regions presented in Figure 19 and Figure 22.

Full scale, elliptically polarized light microscope images were acquired for a total 25 leaflets. Representative samples for each of the three leaflets (left, right, and non-coronary) are shown for comparison along with tracings of the major fiber bundles to better illustrate the major structures (Figure 12). Clearly visible under elliptically polarized light are extensive and complex arrangements of fiber bundles and connecting membranes, i.e., the mesostructure of the leaflet.

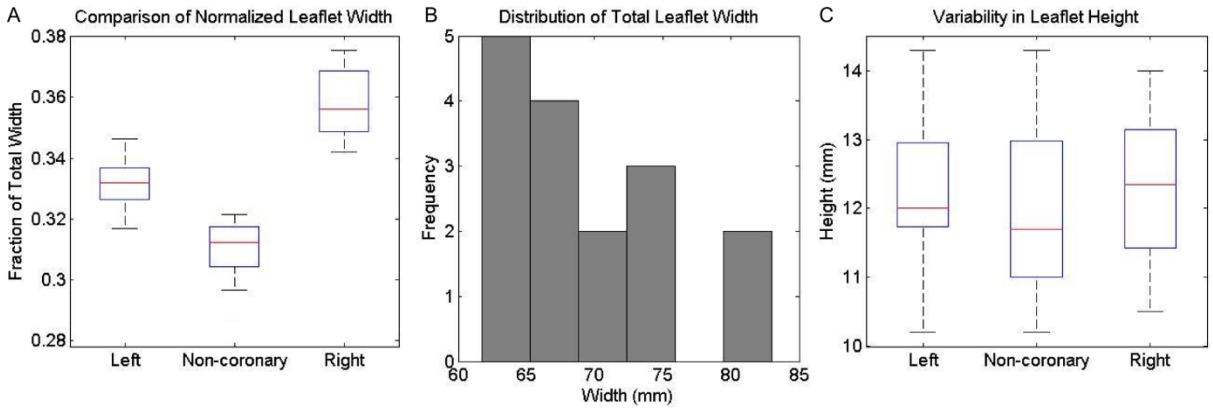

Figure 13 Figures of whole leaflet properties. (A) Boxplot of aortic leaflet widths normalized as a fraction of the sum of the 3 leaflets' widths. The leaflet widths are significantly different from each other with the right coronary leaflets being the widest, followed by the left coronary leaflets and the non-coronary leaflets being the least wide (p <0.01, one-way ANOVA, n = 48). (B) Histogram displaying distribution of total leaflet width for a valve. The distribution is clearly not normal. (C) Boxplot of aortic leaflet heights, where no significant difference was found between the heights of the leaflets (p > 0.05 via one-way ANOVA).

Whole valve-level morphological differences between these three leaflets were readily distinguished using this imaging technique. We observed the right coronary leaflets to be the widest, followed by the left coronary leaflets, and the non-coronary leaflets are the narrowest (p <0.001, Figure 13A). The distribution of the sum of the leaflet widths for a valve, as an approximation of leaflet size, had a non-normal distribution with an average sum of 69.6mm (Figure 13B). The total leaflet width had some weak correlations with N_r and W_r, but none were significant (p >0.05) On the other hand, there were no significant variations regarding their root-to-coapting heights (p >0.05, Figure 13C).

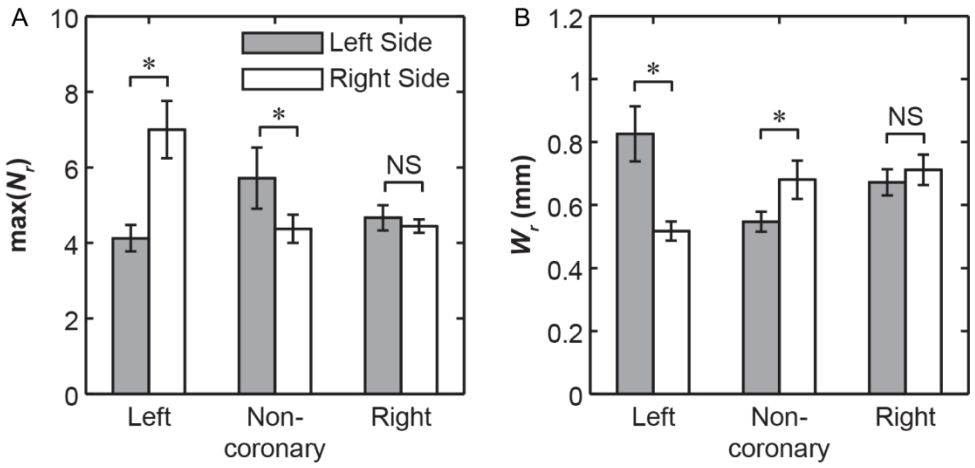

Figure 14 (A) Bar graphs of average fiber bundle counts (max of Nr) for each side of each leaflet (mean ± SEM, *: $p < 0.01$ via student's t-test between each side of the coronary, n = 48). (B) Bar graphs of average fiber bundle width at the root (Wr) for each side of each leaflet. Error bars indicate standard error. The left leaflets had significantly wider fiber bundles on the left side (mean ± SEM, *: $p < 0.01$ via student's t-test between each side of the coronary, n = 239).

The left coronary leaflet was found to be highly asymmetric, as reflected by the unequal number of total fiber bundles max (N_r) on each side (p <0.001, Figure 14A, Appendix Figure 36). In comparison, this structural asymmetry is much less substantial for the non-coronary leaflets, and absent for the right coronary ones (Figure 14A). Each side has on average 5.5 fiber bundles so all figures will analyze only the first 5 when plotting against N_r.

Within each leaflet, the fiber bundles are mostly aligned transversely, mostly parallel to the free edge, except for those at the base, where they take a more radial-like direction (Figure 15). At the nadir, some bundles were observed to travel underneath the others and cross over each other. For the transverse fiber bundles, they extend inward from the root on either side, tapering or branching as they traversed to the middle of the leaflet. Each fiber bundle is composed of well aligned, highly parallel collagenous fibers, similar to other fibrous connective tissues such as tendon [63]. Images also revealed crimp patterns, a common feature for collagen fibers [59] (Figure 16).

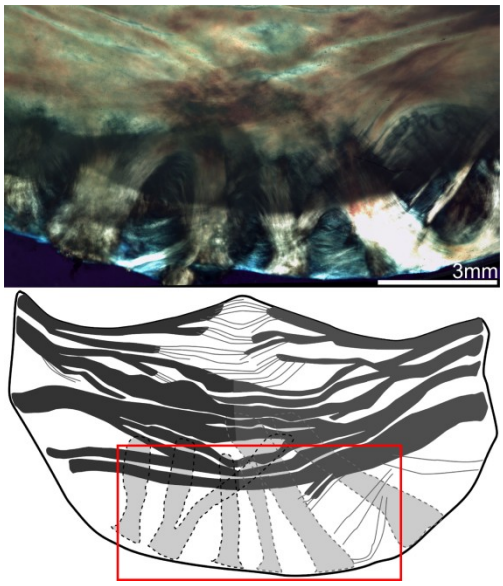

Figure 15 Polarized light image of the right aortic leaflet with trace highlighting the underlying fiber bundles (shown in light grey in the trace) that travel upwards from the nadir of the leaflet.

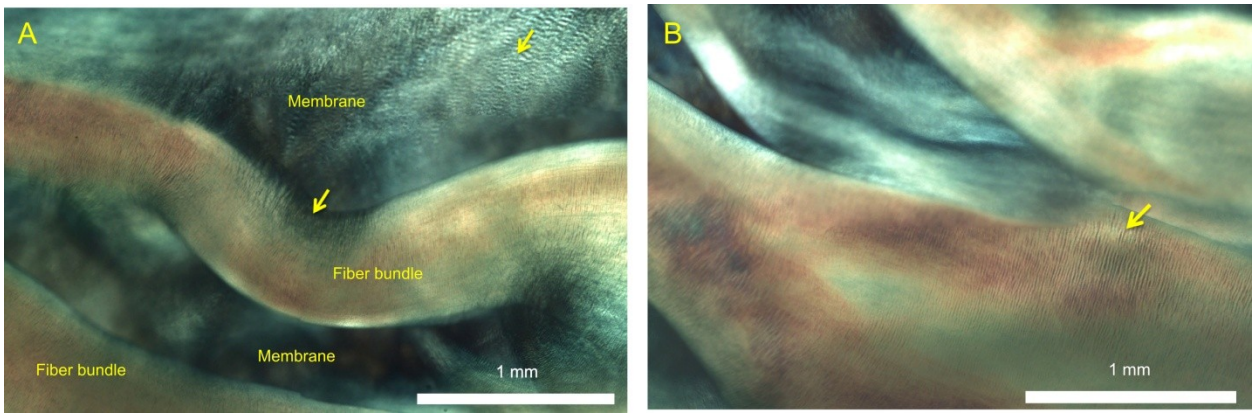

Figure 16 Polarized light images of aortic valve mesostructure. (A) Image of typical fiber bundle (orange) and membrane (blue, blue-green) structures showing the crimping patterns typical of collagen (arrows) and highly parallel fibril organization in the fiber bundles. (B) Image of complex overlapping fiber-membrane structures showing crimping patterns typical of collagen (arrow), as well as the fiber bundles branching and extending inwards from the root of the leaflet, interconnecting with membranes with fan-like and pinnate structures.

We also revealed more structural details of the membranes. The membrane was shown to contain very thin 'sheets' of collagen again with plainly visible crimp patterns (Figure 16A). Often two or more sheets appeared to

'overlap'. In comparison to the highly ordered collagen alignment in the fiber bundles, the membranes displayed a less organized collagen alignment, with multiple overlapping regions of locally parallel fibril bundles (Figure 16B). The membranes appeared to be larger without fiber bundles in the regions close to the free edge, and smaller near the belly.

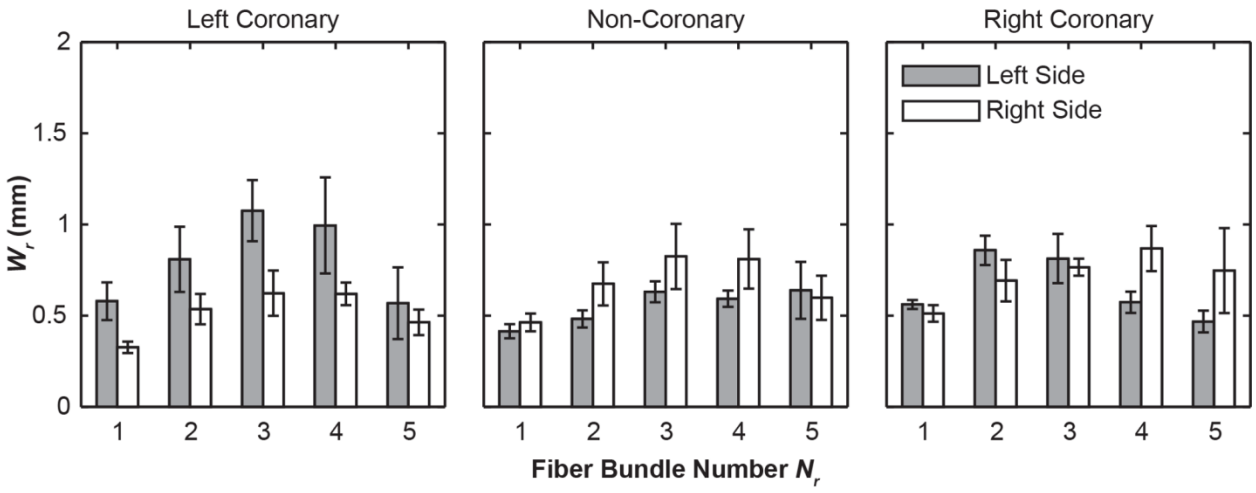

Figure 17 Bar graphs of average fiber bundle root width ($\boldsymbol{W_r}$) as a function of position from the free edge ($\boldsymbol{N_r}$). The fiber bundles toward the center of the leaflet (N_r = 3, 4) tended to be the widest with the addition of the second fiber bundle on the right coronary leaflet. Error bars indicate the standard error.

Within each leaflet, these fiber bundles display significant variations in its root width, W_r. The fiber bundles ranged from 0.174mm to 2.7mm (W_r) in width at the root, whereas the widest bundles were found near center of each leaflet (N_r = 3 or 4, except N_r = 2 for the left side of right coronary, Figure 17). The values of W_r, are significantly greater on the left side for the left coronary leaflet, on the right side for the non-coronary leaflet, and no difference for the right coronary leaflet, as shown in (p <0.0001, Figure 14B).

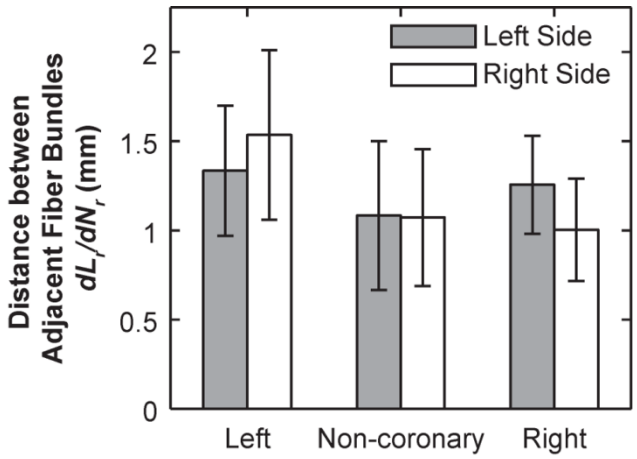

Figure 18 Bar graph of average distance between adjacent fiber bundles on each side (mean ± 95% confidence intervals), calculated by least squared linear regression of L_r over N_r on each side of each leaflet ($\underline{R}^2 > 0.81$ for all regressions).

Overall, the distance between fiber bundles averaged 1.12 mm from center to center at the root. This varied across the leaflets with the left coronary leaflet having larger gaps between fiber bundles relative to the non-coronary and right coronary leaflets (p <0.0001, Figure 18).

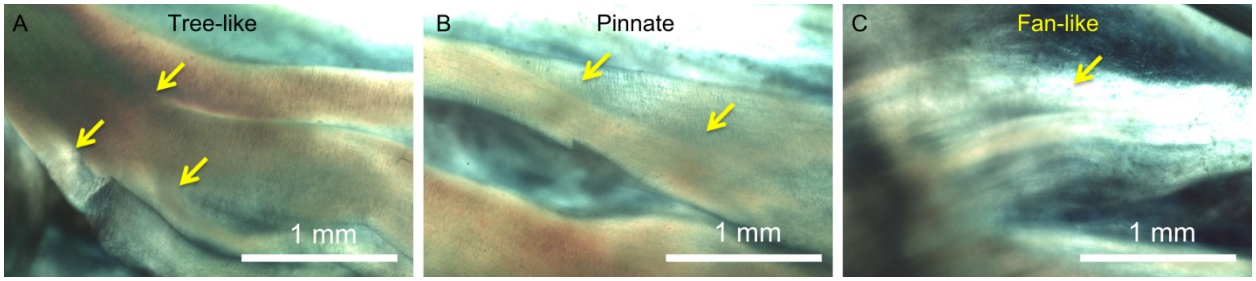

Figure 19 High resolution polarized light images of fiber bundle branching patterns from Figure 15. Three branching mechanisms were shown: (A) Tree-like fiber bundle branching. (B) Pinnate fiber branching. (C) Fan-like fiber branching.

In all of these three leaflets, three distinctive types of fiber bundle branching patterns were observed : 1) tree-like branching, in which each fiber bundle split into 2 or more bundles of similar form (Figure 19A), 2) pinnate branching, where the fibrils of the bundle would start to spread out but maintained some of their parallel organization like the bristles of a brush (Figure 19B), and 3) fan-likebranching, where the bundle completely separated into its constituent fibrils embedding into the underlying membrane (Figure 19C). Among these three modes, the tree-like branching was the most frequent mode, except for those at the nadir, which generally did not

branch out. The pinnate branching mode occurred exclusively near the free edge of the leaflet (bundles of $N_r = 2$ or 3). The fan-like branching appeared exclusively in the fiber bundles nearest to the free edge ($N_r = 1$ or 2). These trends were consistent across the three leaflets.

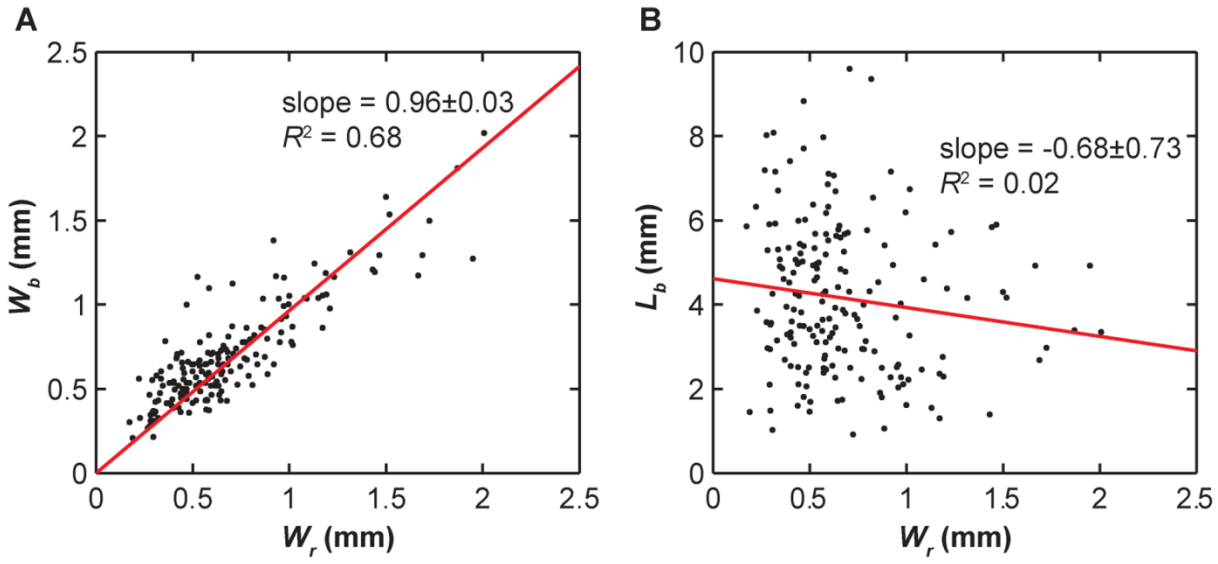

Figure 20 Linear regression of branching measurements. (A) Graph of the fiber bundle width at the first branch point (W_b) relative to the width at the root (W_r). The trend line has an R^2 value of 0.68 suggesting some relationship between W_b and W_r. The slope of the trend line is close to 1 suggesting that the fiber bundles do not widen before the first branch point. (B) Graph of the length along fiber bundle to the first branch point (L_b) relative to the width at the root (W_r). The trend line has an R^2 value of 0.02 suggesting no correspondence.

The fiber bundle width at the branch point (W_b) remained unchanged relative to the width at the root (W_r) (Figure 20). This appears to hold true when comparing leaflets ($p > 0.05$) and left versus right side ($p > 0.05$). However, the fiber bundles widened significantly in the first fiber bundle ($p < 0.0001$, Figure 21). The point of branching of a fiber (L_b) is related to its position (N_r) along the leaflet ($p < 0.05$) but is not significantly related to leaflet ($p > 0.05$), side ($p > 0.05$), or fiber bundle width (Figure 20B, Appendix Figure 37).

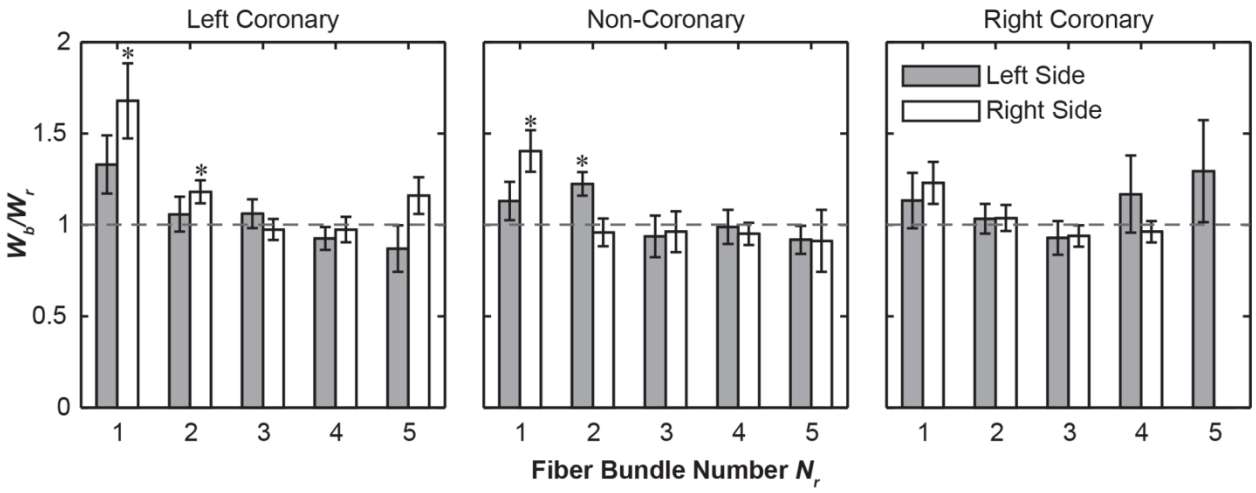

Figure 21 Bar graphs of the relative widening (W_b/W_r) as a function of fiber bundle position from the free edge (N_r) (mean ± SEM). (*: $p < 0.05$ via student's *t*-test).

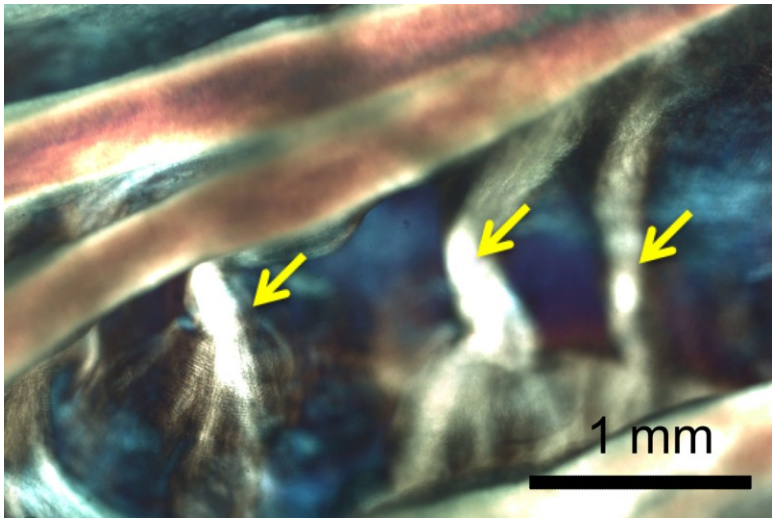

Figure 22 Higher resolution optical image of the left coronary leaflet showing the anchoring structures of fiber bundles, with fibrils branching off into the connecting membrane.

The membranes and fiber bundles appeared in many regions to be connected by an 'anchoring' structure (Figure 22) consisting of collagen fibers that spread from the bundle near the root and extend into the underlying membrane in a manner similar to the fan-like pattern. These structures were observed mostly in the fiber bundles away from the free edge (N_r = 2, 3 and 4). Unlike the branching mechanism, anchoring did not appear to alter the thickness of the main fiber bundle.

2.4 Discussion

The overall goal of this study was to provide a quantitative evaluation of mesoscale fiber and membrane structure of the aortic valve cusp leaflets, which can contribute to the understanding of the structure-function relationships of the aortic valve. To achieve this goal, we implemented a novel computer controlled, automatically focusing imaging system at micron scale resolution, for the purposes of large scale imaging (up to 60,000×40,000 pixels) of fresh (and hence thick) specimens in fluid. Using this approach, we carried out quantitative, detailed structural characterization on individual fiber bundles and their associated membranes. These studies thus provided the quantitative evidences on the complex collagenous structure of the aortic valve that serves as the basis for understanding its loading environment, tissue function and for bioprosthetic designs.

2.4.1 Structure variation between different cusps

Previous work by Dr. Doehring had identified the structural variations between three valve cusps, including the cusp areas, average bundle diameters, and fiber bundle count [59]. In this chapter's study, with the improved imaging technique, we further investigated the cusp-to-cusp structural variations that could provide insights into their different mechanical environments and tissue functions. For example, significant variation in the leaflet width (Figure 13A) could be adaptations for the dynamics of the aortic root during the cardiac cycle [31]. The high asymmetry in the left coronary cusp, including total number of fiber bundles (max(N_r), Figure 14A), fiber root diameter W_r (Figure 14B) could be correlated with the asymmetric tensile and compressive stress executed on the tissue. There is an inverse correlation with the total number of fiber bundles, max(N_r), on each side of the leaflet and the size of the fiber bundles, W_r (Figure 14). This correlation is most pronounced in the asymmetric organization of the left coronary leaflet (Figure 14), which is suggested to be designed in a manner to accommodate the higher compliance of the left coronary leaflet [12]. In comparison, this asymmetric effect is less substantial for the non-coronary leaflet, and insignificant for the right coronary leaflet (Figure 14). The space between fiber bundles was also greatest in the left coronary leaflet which could increase the overall flexibility of the whole leaflet (Figure 18). Dr. Peter Hammer et al suggested that having angle reinforcing fiber bundles served two functional purposes. First, the angled collagen fibers would additionally dampen the transitional stresses caused by the pressure gradient inversion during diastole. Second, as this configuration would force the leaflet to flatten to a greater extent which in

turn would ease coaptation [64]. Taken together, the differences in fiber bundle morphology between the leaflets provided details into how bioprosthetic valves can be designed to emulate the tissue-level heterogeneity of the valve.

2.4.2 Mesostructure of cusp fiber bundles and membranes

This study is the first kind of detailed, quantitative investigation on the mesostructure of the aortic valve fiber bundles and membranes. The results of this study deviate from the commonly used, tri-layered model of the aortic valve structures [10, 36]. As our previous work [59] acknowledged the complexity in the structure, this study further investigated the sub-tissue-level features. This highlighted the high complexity and asymmetry of the cusps, which likely reflects the optimizations of its tissue function.

In particular, we found that the fiber bundle diameter is largest in the middle of the leaflet, decreasing as bundles are closer the free edge or nadir of the fixed end (Figure 17). This is consistent with previous observation that individual fibril diameter increases traversing from the fixed edge of the leaflet to the free edge [11], and the fiber bundles roughly equidistant from the lowest point of the root and the free edge are the thickest [59]. These results together suggested that the fiber bundle diameter is dependent both on the number of fibrils and their diameter. This higher W_r and smaller membrane regions may be an adaptation to the peak stress and strain occurring in the belly of the leaflet [31]. It is also correlated with the presence of additional anchoring structures supporting the bundles in the high strain regions.

In addition, the fiber bundles were found to maintain a consistent thickness as they travel from the root (W_r) to their first branch (W_b) (Figure 20A and Figure 21). This feature is beneficial in homogenizing the stresses through the fiber bundles and preventing loading spikes. One exception is that we always observed widening at the branching point for the first bundle for the left and non-coronary leaflets (N_r = 1, Figure 21A, B), which is likely a result of fibril dispersion in the branching patterns other than the “tree-like” mode (Figure 19). In addition, the distance from the root to the first branching point (L_b) was found to be independent of the root thickness W_r, (Figure 20B) the leaflet, and the side of the leaflet (p >0.05, data not shown).

Besides the variation in each fiber bundles, we also identified the various configurations with how the fiber bundles branch and interact with their adjacent membranes, including the ‘anchoring, ‘tree-like’, ‘fan-like’, and

'pinnate' fiber branching patterns (Figure 19). While tree-like branching was reported previously [59, 65, 66], to our knowledge, it is the first time that the distinctive anchoring, fan-like, and pinnate branching structures were reported. Interestingly, over the 25 leaflets tested here, we did not observe the "fractal" branching pattern that was described previously [65].

The tree-like branching was be the dominate branch form towards the belly of the leaflet. Driessen et al had previously mapped out the overall collagen alignment through a leaflet and found that the collagen is more uniformly aligned circumferentially close to the free edge where the loading is more uniaxial. However, the tissue was loaded more equibiaxially in the belly region and deviation in the overall alignment [67]. The tree-like branching produces collagen fibers oriented less circumferentially which can better serve to carry biaxial loads.

The anchoring structures occurred close to the aortic root. We speculate that they serve to facilitate a smooth transfer of stress between the aortic root and the leaflet. Dr. Mano J. Thubrikar et al published a study highlighting the important of the stress sharing between the sinus and the leaflet to the longevity of the valve. The failure of this transfer could result in pulling on the region between the leaflets which may contribute to permanent bending observed in the stent post of some bioprosthetic valves [68]. The anchoring structure may also keep the attached fiber bundle from shifting at the root so the fiber bundle remains running circumferentially.

Overall, these variations in the fiber bundle morphology indicated that there are many 'pathways' to a functionally successful valve with respect to specimen-specific leaflet mesostructure. These results also indicated that mechanics (hemodynamics) may play a significant role in valve development. It is likely that genetics provides the 'initial conditions' for the valve's basic morphology, and then the valve develops and remodels over time *via* biomechanical influences that 'fine-tune' a final optimal structure for the individual. Further studies on the genetic conditions and biomechanical environments are required to fully understand the origins of this mesoscale heterogeneity.

The commissure is thought to be the major shock absorbing region which transfers the load to the aortic wall [69]. This may be what encourages the fan-like and pinnate morphologies where the fiber bundles separate into their constitutive fibrils. The collagen fibrils being more dissipated over the membrane allow for the membrane to be

uniformly reinforced and unlikely to tear. The more wavy shape of the fan-like branching may give it more capacity to absorb recoil and strength as upon stretching the fibrils would then straighten [69]. Additionally, these branching patterns serve to flatten the fiber bundle by distributing it over a larger area. This in turn should allow for a better commissure to commissure seal between the leaflets compared to if the fiber bundles were rounded. This mechanism would also explain why the fiber bundles have a smaller width as they approach the free edge.

2.4.3 Autofocusing imaging technique

A key aspect of this custom imaging system was the implementation of a novel auto-focusing algorithm. Most current auto-focus systems employ a contrast based method, using either center focusing or spot-arrays. Previous contrast method often produced inconsistent results and out-of-focus images for specimens with large and heterogeneous thicknesses. In this study, we applied an edge detection based algorithm which uses the entire image to achieve an optimal overall focus in a consistent fashion. The net effect is the substantial increase in image resolution (~ 0.86 μm/pixel) over our previous publication (~ 14.8 μm/pixel) [59]. This improved design allowed detailed quantification of the heterogeneity of these leaflets at both whole tissue and fiber bundle levels presented here. Besides its application to the aortic valves, this method also holds great potential for studying the mesoscale features of other collagen-based connective tissues, such as tendon.

2.4.4 Limitations and outlook

We identified several technical limitations of the method that can be further improved. Firstly, there is no automatic modulation of the exposure in the software, which leads to over-illumination of relatively thinner regions, and lack of illumination in thicker regions. Secondly, the stitching program sometimes resulted in minor misalignment. However, as we found most images are well-aligned, we expected these technical issues to have minimal effect on the data or any conclusion in this study. We are currently working on improving the high-dynamic-range capability and stitching algorithm that numerically guarantees pixel accurate whole valve (or any specimen) alignment. It should also be noticed that the presented focusing method is slower compared to contrast methods (appx. 10-20 seconds per focus).

It is known that the porcine aortic valves bear some non-trivial structural differences with human aortic valves. For example, the relative size of the leaflets varies between the species. In porcine aortic valves, the right coronary leaflet has the most surface area and the non-coronary leaflet has the least. In human valves, the non-coronary leaflet has the largest surface area and the left coronary leaflet has the least [14]. Thus, the data presented here may not be directly applicable when considering the structural heterogeneity of the human aortic valves. If sources of human aortic valves are available, our future studies will focus on characterizing the structure of human samples with similar and improved imaging techniques, which in hope will provide direct insights into the design and function of human aortic valves In addition, we are studying the loading dynamic of the fiber bundles and membranes individually, which could integrate with the structural analysis and better understand the structural and mechanical design principles of aortic valves.

2.5 Conclusions

In this study, we applied a novel polarized optical microscopy technique with sub-micron resolution to reveal the mesoscale structural heterogeneity of collagen-fiber based porcine aortic valves. We discovered and quantified the structural heterogeneity between left coronary, non-coronary and right coronary leaflets, at both whole-tissue and fiber bundle levels. Detailed structure of the collagen fiber bundles was revealed, including fiber bundle alignment, branching mechanism and heterogeneity within each of the leaflet. The structure of the less organized membrane and fiber-membrane anchoring mechanism was also investigated. These structural features are suggested to be highly correlated with the biomechanical function of the heart valves. These new insights are valuable for developing more precise models as well as aiding in development of improved, long lasting tissue-engineered, bioprosthetic, and synthetic valve replacements.

Chapter 3: Development of a Uniaxial Testing System

3.1 Introduction

One of the major obstacles to mesostructure mechanical analysis is having an appropriately scaled testing system. The specimens undergo non-uniform deformation which necessitates a direct strain measurement as opposed to using the applied displacement and initial length. Thus, the work presented in Chapter 4 on the mesostructure biomechanical properties could not be done with a commercial testing system. To order a complete custom made system to be created would cost on the order of hundreds of thousands of dollars. To that end, we developed a low-cost testing system that readily interfaced with a standard microscope. The resulting system allowed us to capture video and load data of specimens on the size order of 6 mm length by 4 mm width during uniaxial displacement tests.

3.2 Design Requirements

The following are the design criteria were used to create and evaluate the testing system:

1. **Testing device must be capable of fitting on a microscope stage** – This allows the device to be readily integrated with the microscope to take advantage of the image acquiring capabilities. This limits the dimensions of the testing device to an area of the microscope stage and a maximum height is 3cm.
2. **Load or displacement control** – This is a general prerequisite to any sort of biomechanical testing system, there must be a means to induce strain on the specimen.
3. **Minimal damage to specimens** – The system must avoid tearing the specimens at the points they are held as this would invalidate the results. The specimens must also be kept hydrated as dehydrating collagen can cause it to break easily and significantly modifies its biomechanical properties [70].
4. **Acquire load data with minimal noise** – The precision of the system's measurements would be reduced by a poor signal to noise ratio of the load data.
5. **Synchronized motor activity, video/image acquisition and load data acquisition** – The motor's activity, video images, and load data must be organized in time to allow real conclusions about load-displacement data.

6. **Keep the camera images in focus and centered on the specimen** – As a specimen is stretched, the focal plane may rise or drop resulting in out of focus images without compensation. Additionally, if one end of the test system is fixed, the region the camera was recording will start to migrate especially during high strain (>50%) tests.

3.3 Testing Device

We have developed two testing devices. The original testing device made use of a steel cantilever beam as its load transducer as shown in Figure 23A. On this beam, there were 4 strain gauges which comprised a full Wheatstone bridge circuit described in Figure 23B. The appeal of this design was its high sensitivity for smaller specimens. The cantilever beam and the stepper motor were held onto an aluminum frame. Custom steel clamps were machined capable of holding specimens on the order of 1-4mm in width. One clamp went to the lead screw of the stepper motor while the other went to a bearing on the cantilever beam. The beam was designed to be stiff enough that even our highest anticipated load of 20N would produce less than 0.5mm of beam displacement.

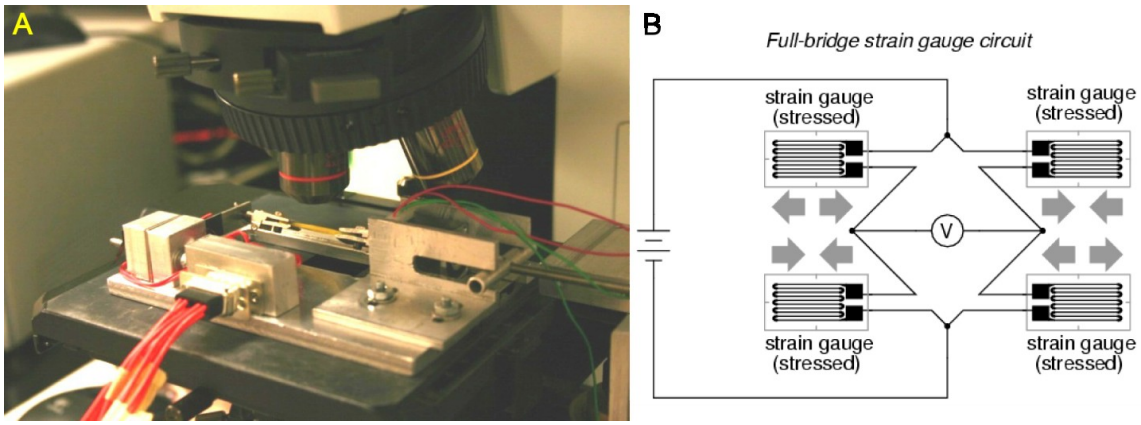

Figure 23 Cantilever Testing System. (A) Image of cantilever testing device on microscope. (B) Circuit diagram of full Wheatstone bridge strain gauge circuit.

The second testing device was designed with for heavier load testing. The strain gauge sensor was replaced with a load cell rated to 25N force. The entire frame was redone to be more robust and stable. The stepper motor is now vertically supported by a slider which holds the lead screw through the motor at a set height. The same steel clamps are used one of which is attached to a universal bearing to permit specimen rotation. A diagram and image of this

testing device is shown in Figure 24. This second device was the one used in this thesis for the rest of Chapter 3 and all of Chapter 4.

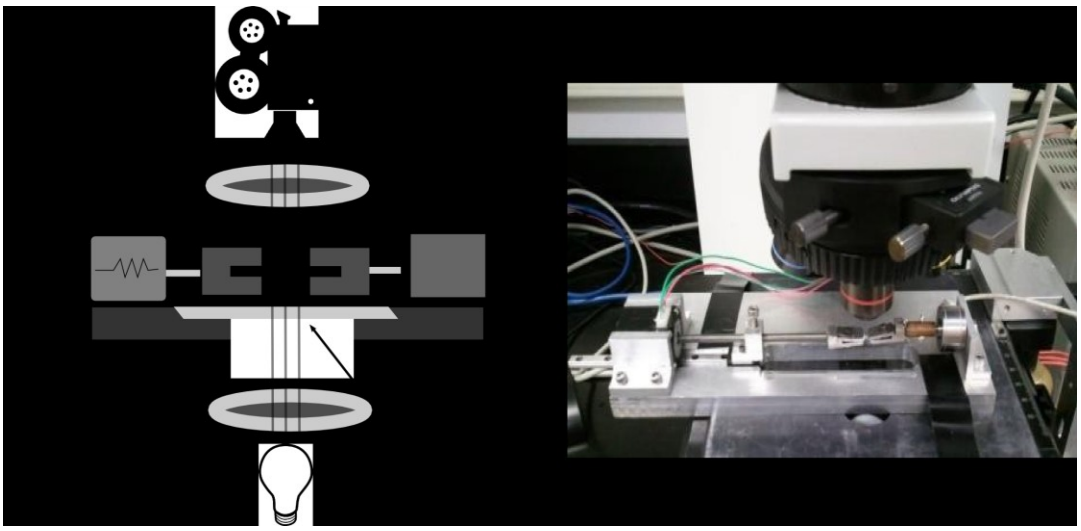

Figure 24 Load Cell Testing System: (A) Schematic of micro-testing system. (B) Photo of testing system on microscope. The testing device fits on top of a microscope outfitted with a camera. A specimen is held in a pair of clamps. One clamp is attached to a load cell to observe the force applied to the specimen. The other clamp is attached to a stepper motor which provides the displacement. Two polarizers transform the transmitted light, giving it an elliptical polarization. The microscope's base is motorized in the x and z directions allowing the specimen to be kept in focus and centered in the field of view.

3.4 Electronics

The system has two computers: a master controller and a motor server. The master computer initializes the tests, collects the image/video feed from a Pixelink®[71], and data from a Labjack U3 I/O Device[72]. The Labjack polls the system at an average rate of 200 samples per second. The other computer acts as a server to the motors passing along the commands from the master computer. Communication between computers is done via a serial port connection. Images are acquired using a Pixelink® digital camera integrated with the microscope. The microscope that this system is on has been previously set up for 3 axis stage movement. This configuration can be seen in Figure 25A and is summarized in Figure 25B.

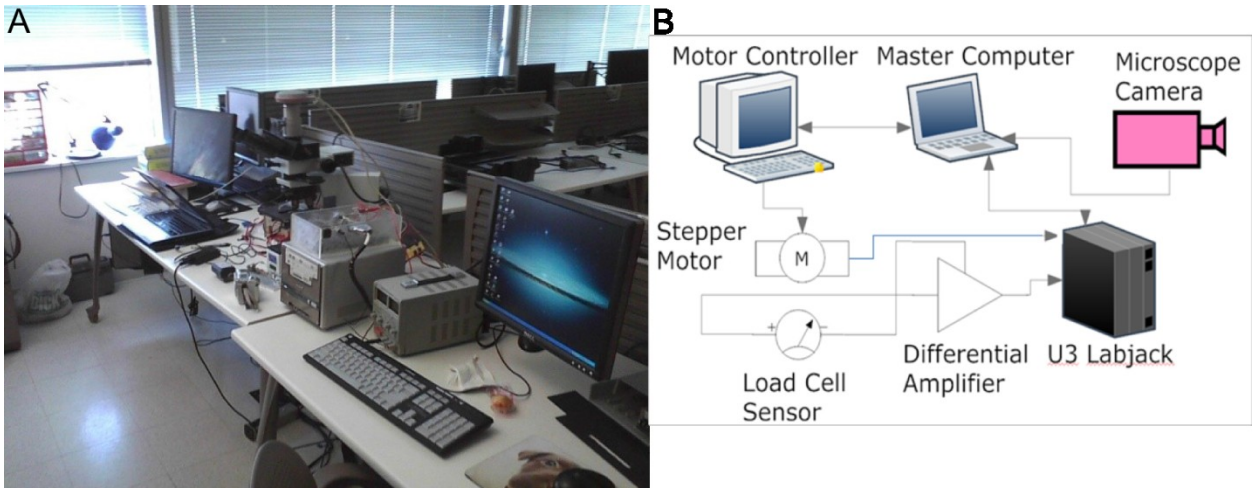

Figure 25 (A) Photo of Lab Setup. (B) Schematic Overview of Testing System.

The stepper motors of the stage and testing device are all controlled by an Ability Systems' Indexer LPT®[73]. The Indexer LPT gives us the ability to engage all of the motors at the same time and control the speed in terms of steps per second. The interface with the motor controller computer is through a parallel port connection with latency on the order of milliseconds.

With both the cantilever beam device and the load cell device, the load data was determined by the difference of two voltage signals. Each signal is boosted and some of the noise is filtered out by a 741 unit gain amplifier circuit. These signals are then passed as input to an INA 101 differential amplifier circuit. The gain of this circuit and offset of this system determine the output which is passed onto the Labjack for digital conversion.

The system directly monitors the activity of the device's stepper motor to ensure synchronization between the load cell data and the motor. When directly sampling the voltage of the motor, the signal noise in the Labjack dramatically increases. To work around this, the system uses opto-isolator circuit to monitor motor activity. This consists of an LED and resistor in parallel with the stepper motor's supply voltage and a photo resistor across from the LED. When the motor is activated, the luminescence of the LED changes, producing a clear signal in the opto-isolator circuit's output.

3.5 Programming and Graphical User Interface

The software of this system is predominantly coded in Matlab. The exceptions are several C++ applications that are used to interact with the Pixelink camera and one which polls the computer clock. The video/image and Labjack data are synchronized using parallel processes of the same C++ application which polls the computer clock for the designated time to start the trial. The effectiveness of this method has been verified by comparing known video events (the start and stop of motion) with load cell events (the start and stop of loading). The timestamp of these events agree to the precision of the video's frame rate.

There two modes of testing were created: 'continuous' and 'sequential', labeled "fast" and "slow" on the Master GUI in Figure 26. Continuous testing mode pulls the specimen without pausing while the camera captures video images at 5-20 Hz depending on exposure time and image size. This mode better preserves the viscoelastic load compared to sequential tests. Sequential tests pull the specimen a fraction of the total displacement based on the number of image frames to be captured. The system then holds the specimen still for image acquisition. The advantages of this method are that there is no limitation of exposure time or camera bandwidth and more sophisticated specimen focusing can be done. This method cancels motion blur but also any viscoelastic data is lost as the specimen is allowed to relax.

As mentioned in the design requirements, specimen regions of interest must be kept as centered as possible in the camera field and in focus. Focusing in the sequential testing is done manually as the whole system is held still before imaging. For the continuous testing, specimens are stretched to half the displacement of the intended trial. Then, the user focuses the specimen using the z-axis stepper motor. The number of steps to focus is stored and then the system is reset to the original position. If "Halflinear" is specified in the Master GUI, for the first half of loading, the stage will rise or fall the number of steps stored and then the second half of the loading has no stage height manipulation. If "Linear" is specified in the Master GUI, the entire loading will have the stage rising for a total number of steps equal to double the amount stored when focusing at half displacement. This has proven an effective means to improve focusing in our preliminary trials.

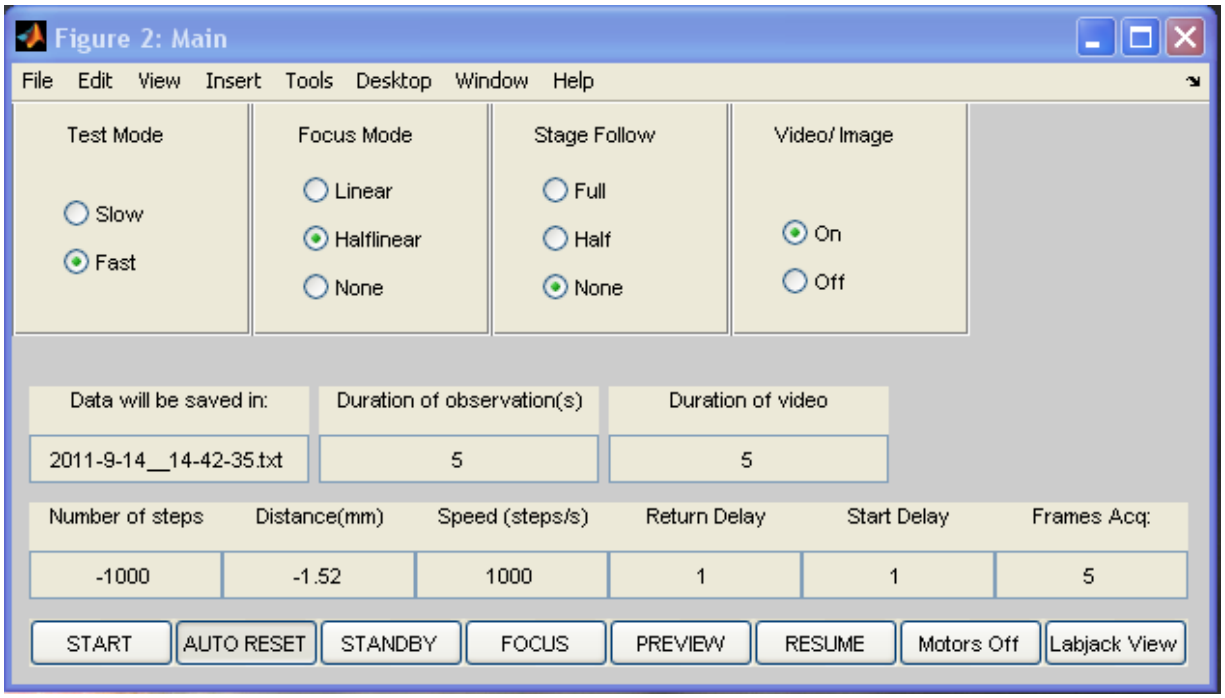

Figure 26 Screen Capture of the Master GUI: Test Mode indicates the type of testing to be done. Focus Mode indicates what if any focusing algorithm is applied. Stage Follow indicates the type of stage movement that will be done. Video/Image data can be turned on or off. The other inputs specify filename, how long load cell and video data is acquired, the amount of displacement, speed, delay before loading, delay after loading, how many image frames are to be captured

To maintain specimen centering, the system uses a stepper motor to move the stage and with it the device in the opposite direction of the device displacement. The stage follow option specifies if the stage displacement to specimen displacement is a 1:1, 1:2, or 0:1 ratio. These two options are chosen by radio buttons in the Master GUI as shown in Figure 26.

3.6 Optical Tracking

The video data is processed using Matlab software developed by Dr Doehring to track features from the image series and calculate strain fields. Color video is acquired during the test. At 4x magnification, the camera resolves 1 pixel at 1.2μm^2 in a non-decimated image. This is processed in Matlab by first converting to grayscale and then increasing contrast to enhance 'trackable features'. A distinct advantage of our system (as opposed to other systems that use LabView or other custom software) is that we can take advantage of the full image processing capabilities

of Matlab and design specimen-specific image processing routines as needed. This technique has been previous used to approximate strain is soft tissue specimens during uniaxial loading [74].

3.7 Calibration and Initial Validation

The system has been configured for two different gains in the differential amplifier circuit. The system was calibrated using hanging weights. The average sensitivities are 1.215 mV/g or 123 mV/N and 2.72 mV/g or 277mV/N. Through the calibrated region, the noise band remained ±1g. The load cell was tested up to its functional limit of 25N with the testing device showing a consistent linear response to increasing load.

The initial validation was performed using 3 different springs and a rubber band. The stiffness of each was estimated using a camera and hanging weights to get load-displacement data. These same springs and rubber bands were then put into the testing system and stretched for the same displacement as was observed with the hanging weights. The load-displacement data from the testing system calculated stiffness within 5% of that in the springs and within 10% of that calculated in rubber band when using the hanging weights.

3.8 Evaluation

The final validation of the current system was testing rubber band and cotton fiber specimens. Cotton fibers are viscoelastic, birefringent, and should have non-affine deformation. These characteristics are all shared by the collagen fibers of the human heart valve. Rubber was chosen to represent a homogeneous, linear-elastic material. Thus, we could expect a relatively uniform strain from this simple tensile test experiment.

The cotton fiber specimens were cut to 4.8mm in width and 25mm in length. The rubber band was 5mm in width and also cut to 25mm in length. Each specimen was clamped with 19mm between the clamps. Next, each specimen was displaced 4.75mm at a rate of 1.52mm/s and held at that displacement for 30s before returning to the original displacement. The cotton fiber specimens were stretched prior to each sequential test to maintain tension. These specimens transmitted relatively little light so top-down illumination was used. This provided sufficient light for the low exposure time needed with continuous/video testing. Video was acquired at a rate of 10 frames per second.

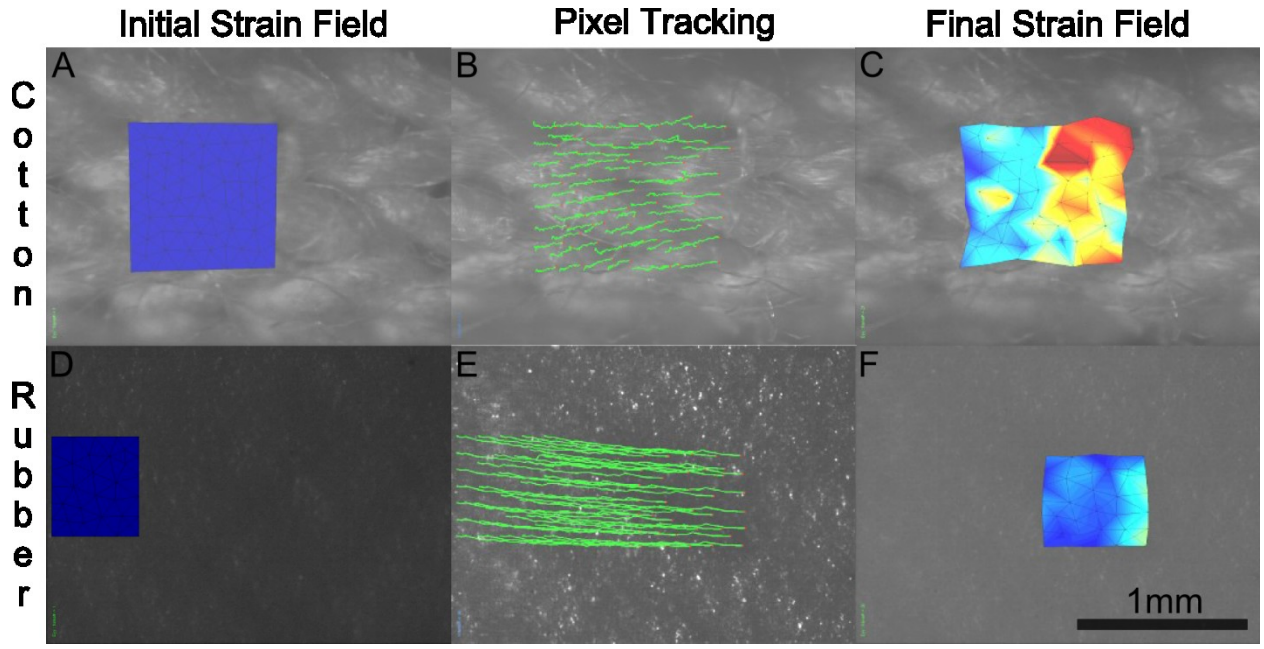

Figure 27 Tracking images of cotton fiber and rubber tests. Images of surfaces using top-down illumination at 0 strain showing the initial selection of points.(A and D) Tracking of pixel points through the trial using Matlab.(B and E) The cotton fiber points on the left side showed lower displacement indicating some success with centering during the test while all the points on the rubber band were clearly shifting. Strain fields of triangles formed by the tracked pixels at the end of the test. (C and F) The rubber was far more uniform in the surface displacement. Despite the loss of centering in the rubber band test, the software was able to compensate for all of the pixel points

Figure 27 shows the optical tracking output and estimated strain fields of the rubber band and the cotton fiber. The cotton specimen had highly regional deformations as the fibers lengthened while the rubber band had a very homogenous strain field. These are consistent with non-affine and affine deformations. At the end of the test, the estimated mean strain of the cotton fiber and rubber band were 17% and 23% respectively. By the third test, the cotton fiber was 27mm long making 17% an accurate strain estimate for a 4.75mm displacement. No change in the strain field appeared during specimen relaxation.

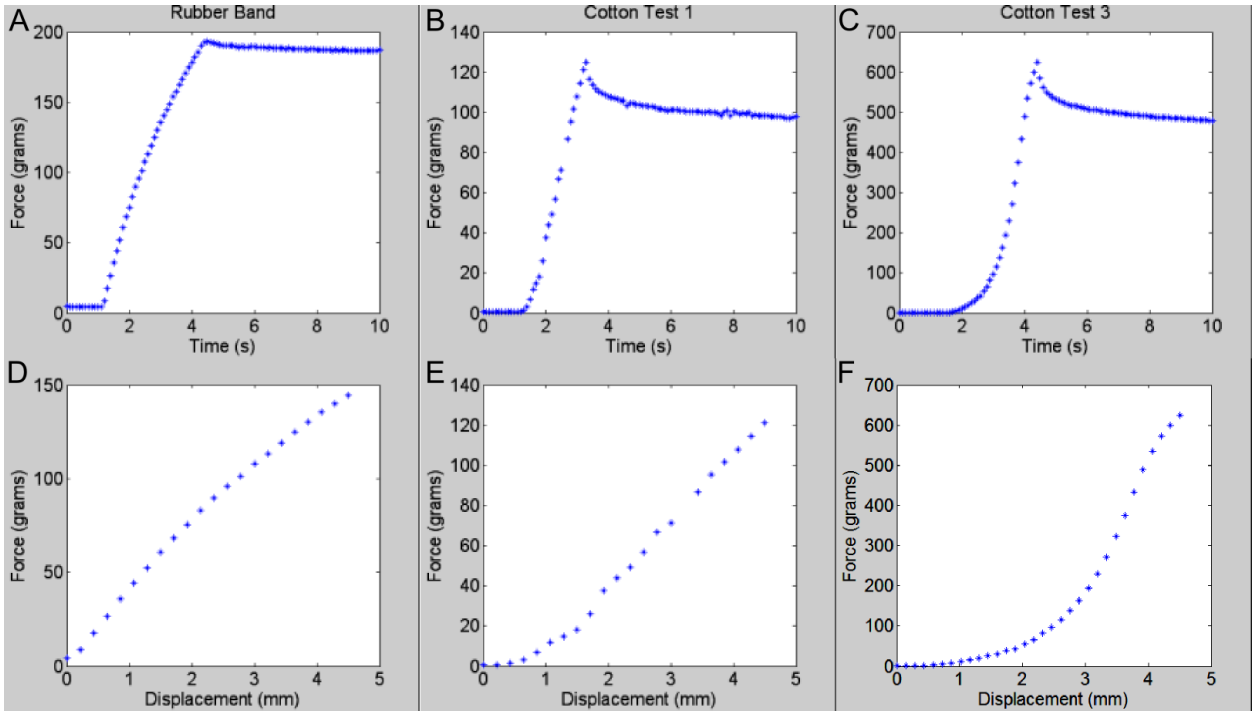

Figure 28 Force-time (A, B, C) and force-displacement (D, E, F) data of rubber band and cotton fiber specimens in stretch and hold tests. Only the first 10 seconds are depicted. The cotton fiber underwent 3 tests with the first and third depicted. Between each cotton trial, the specimen's initial displacement was increased to maintain tension. The rubber band mostly behaved like a linear elastic material having a relatively straight force-displacement curve. The cotton fiber showed a viscoelastic relaxation as well as a non-linear loading curve. As the cotton fiber specimen became more stretched, the peak load increased.

The resulting load-time and load displacement data are shown in Figure 28. The rubber bands suffered no permanent deformation with a relatively consistent stiffness through the test. The cotton fibers showed non-linear load-displacement curves and relaxation during the hold. Having been able to acquire stress-strain and stress-time data for a linear-elastic material and a non-linear elastic, viscoelastic material, we were ready to conduct preliminary tests on aortic valve specimens.

3.9 Preliminary Heart Valve Testing

3.9.1 Materials and Methods

The aortic heart valves from two porcine hearts were extracted. The aortic leaflets were dissected out trying to preserve as much of the base of the leaflet as possible. Six 8mm specimens were cut out of the leaflets with a

scalpel. Five specimens were isolated fiber bundle segments and one was cut across two fiber bundle regions to isolate a membrane region. Additionally, one larger specimen was dissected out containing both membrane and fiber fascicle regions. Each of the specimens were glued in the clamps and stretched 1.5mm at a rate of 0.3mm/s. They were held at this displacement for 30 seconds before being returned to the original displacements. Specimens were kept moist with PBS.

3.9.2 Results

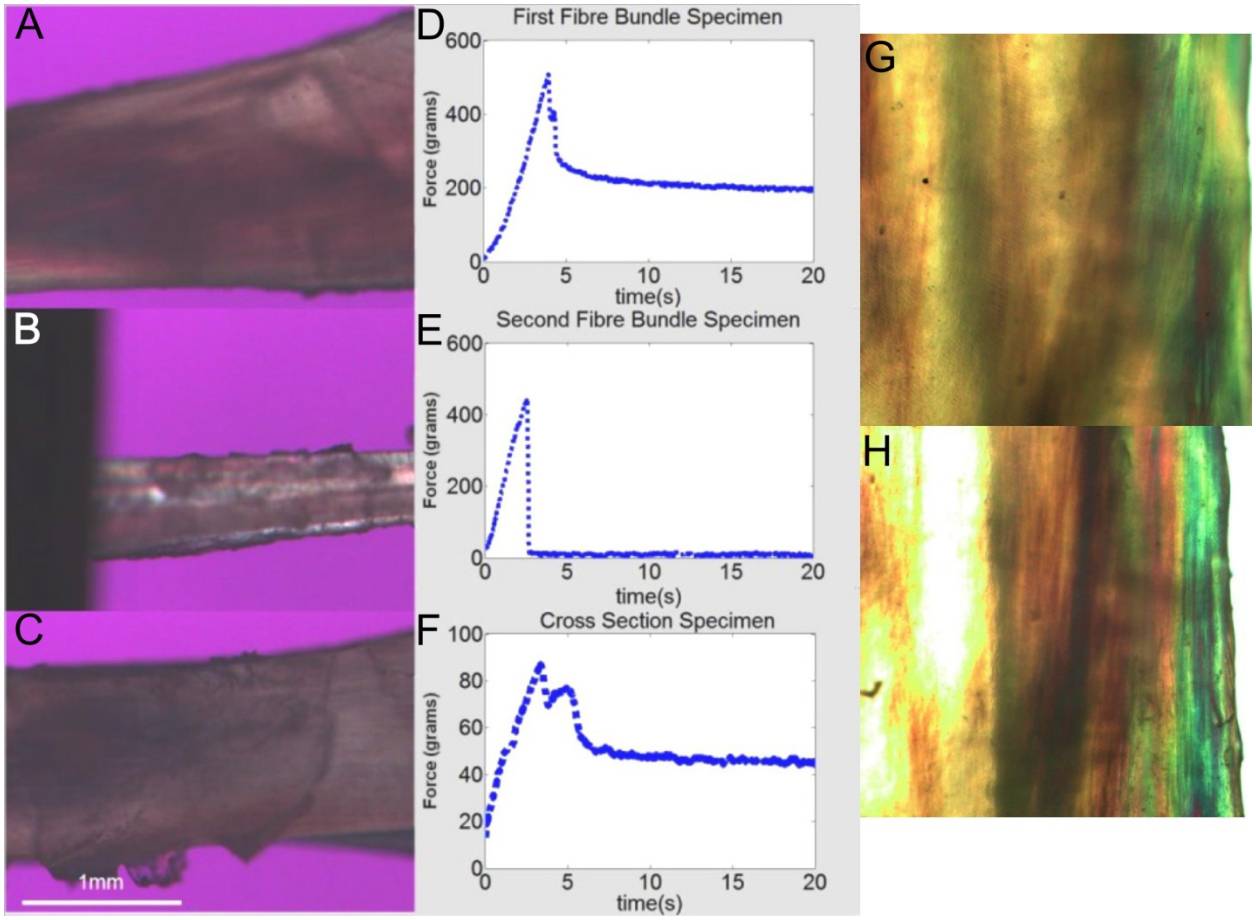

Figure 29 Images of fiber bundles (A and B) and membrane regions(C). Load-time data for the first 20 seconds of the trials: D) The first fiber bundle had a peak load of around 500g. E) The second fiber bundle showed a similar loading curve but then snapped at around 450g load. F) The membrane specimen showed a peak load of only 90g suggesting a significantly less rigid material. Each intact specimen showed relaxation during the hold phase of the test. Porcine valve leaflet images: G) Unloaded sample. H) Loaded sample showing increased fiber alignment.

Of the six smaller specimens, only three did not slip out during testing. In later testing, this was reduced by first gluing the ends of specimens to a wrapping of masking tape and then gluing the tape to the clamps. Figure 29 shows the images and load-time of the fiber and membrane specimens. The collagen fibers are clearly defined. As expected, the membrane region specimen had significantly smaller peak load than the fiber bundle specimen. As the system was not designed for specimens over a centimeter in width, no load data was gathered about the larger leaflet sample. However, the images in Figure 29G and Figure 29H demonstrated the ability of the system to take advantage of the birefringence of collagen fibers and observe the collagen realignment.

3.10 Review of Design Requirements

1. **Testing device must be capable of fitting on a microscope stage** – As shown in Figure 24, the device had been appropriately sized to fit on a microscope stage and hold specimens at a height so they can be viewed by the microscope's camera.
2. **Load or displacement control** – This system achieved displacement control by stretching specimens using a stepper motor which moves a lead screw a set distance with each "step". Each step was roughly 1.5µm. The other side of the specimen was fixed.
3. **Minimal damage to specimens** – This was done using flattened clamps with the specimens glued to strips of paper to create a clamp point. Specimens were hydrated by readily dripping PBS to the point of the fluid remaining on the clamps.
4. **Acquire load data with minimal noise** – This criterion was achieved in the differential amplifier circuit by incorporates a capacitor to eliminate some of the electronic noise generated by the motors.
5. **Synchronized motor activity, video/image acquisition and load data acquisition** – By monitoring the electric activity of the stepper motor using an opto-isolator circuit, the activity of the motors (start of displacement) can be linked in time to the load data. We evaluated the delay between the motor data and the video data and found no significant latency between them.
6. **Keep the camera images in focus and centered on the specimen** – The custom GUI has functions to help preserve image focus by extrapolating linearly from the change in focal height from zero displacement to 50% displacement. The GUI also has functions to move the stage as the specimens are displaced which keeps the same region of the specimen in the field of view.

Having met each of our design criteria and accomplished a preliminary testing of aortic valve specimens, the system was reliable enough to proceed with mesostructure biomechanical testing.

Chapter 4: Biomechanical Testing and Analysis

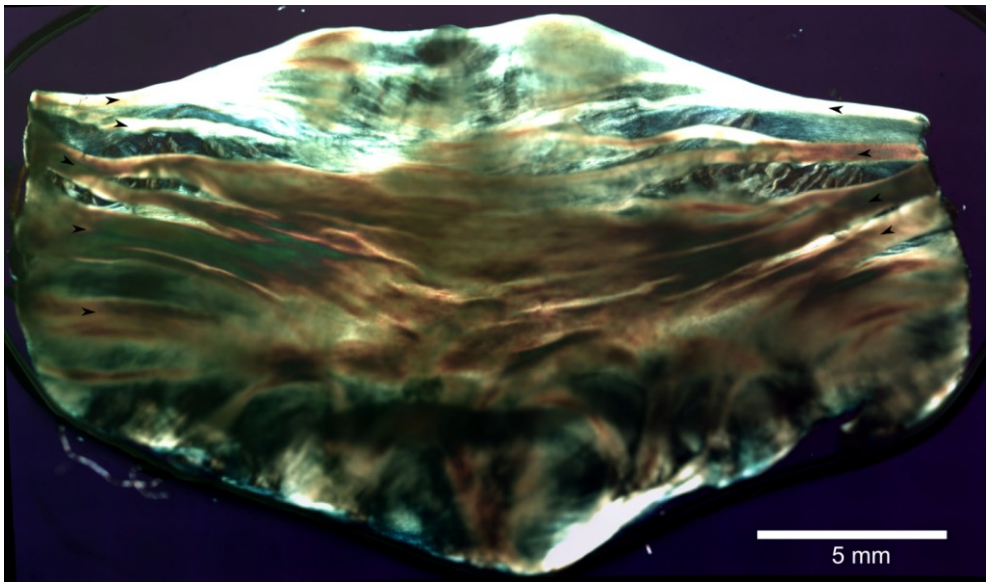

Figure 30: Elliptically polarized light image of a whole right coronary aortic valve leaflet. The fiber bundles run circumferentially (black arrows) with relatively thin membranes between them.

4.1 Introduction

The aortic valve functions to control the direction of blood flow preventing backflow into the left ventricle. The valve has three leaflets (left coronary, right coronary, and non-coronary) each with complex arrangements of collagen fiber bundle and membrane structures. The fiber bundles run predominantly in a circumferential direction [64] with relatively thin membranes connecting the bundles (Figure 30). These structures are likely biologically and biomechanically optimized to provide essential strength, flexibility, and long-term durability for efficient blood flow. In Chapter 2, we explored and imaged these fiber bundle and membrane structures using a novel elliptically polarized light imaging method [59, 75]. This chapter presents new images and biomechanical testing data describing the properties of these valve *mesostructures*; which we define as structures (e.g. fiber bundles and membranes) of size order between the microscopic (cellular) and macroscopic (valve leaflet) scales.

The aortic valve supports high tensile strains (up to ~20% in local regions), tensile stresses (up to ~750 kPa), and shear stresses (up to ~7.9 Pa) at high pressure with rapid duty cycle; ~ 50 ms [8, 76-78]. The valve is highly

anisotropic, with hierarchical extracellular matrix mainly consisting of type I collagen fibers, elastin and other proteins/proteoglycans [8]. The fiber bundles are anchored to the periphery (or 'root') and lengthwise attached to the membranes and coapting edges to form the complete valve. These fiber bundle and membrane mesostructures are suggested to provide the valve with its unique biomechanical capabilities [59].

Bulk biomechanical properties, anisotropy, and heterogeneity of aortic valves have been previously described in many studies [31, 35, 37, 79-81]. Leaflet specimens have been found to be stiffer with less relaxation in the circumferential direction (along which most collagen fibers are aligned) than the radial direction [37]. Leaflets are often described having fibrosa, ventricularis, and spongiosa layers. The fibrosa is the stiffest due to the higher fiber/collagen content compared to other layers [35]. Current understanding of aortic valve biomechanical properties is primarily based on tests of whole leaflet specimens (both radially and circumferentially oriented) and the three constitutive layers [36, 66, 80, 82, 83]. Notwithstanding these efforts there have been, to our knowledge, no studies that specifically investigated the biomechanical properties of the fiber bundle and membrane mesostructures, or the biomechanical heterogeneity within each valve of these structures. In this study, building upon our image-based structural analysis of the aortic valve at the sub-mm level from Chapter 2, we developed a custom uniaxial tensile micro-testing instrument, as discussed in Chapter 3, and have begun to quantify the biomechanical properties of porcine aortic valve fiber bundles and membranes.

The unique and complex structure of the valve is likely the result of a combination of genetic, developmental, and biomechanical factors [75]. When testing and analyzing these highly non-uniform, anisotropic tissue specimens, end-to-end clamp displacement was not an ideal strain measure. Indeed, deformations often appeared to be non-affine, with fiber bundles sliding and reorienting into the direction of loading. To address this issue, we used novel polarized light imaging and image correlation techniques to directly measure strain in the central region of the specimens. Using code and a GUI developed in-house, fibers visible in the images/videos can be selected and 2-D deformation strain fields (for each structure) directly computed.

Detailed understanding of the valve architecture and component biomechanical properties can lead to better understanding of valve properties in both normal health and disease. The ultimate goal of this work is to provide biomechanical and image-based data regarding the main mesostructures (fiber bundles and membranes), comparing

properties between the three leaflets and the two sides of each leaflet. Linear, non-linear elastic and viscoelastic properties were estimated from controlled stretch-and-hold tests. This information can facilitate development of improved valve replacements, bio-constructs, and better overall understanding of valve structure-function relationships.

4.2 Materials and Methods

4.2.1 Specimen preparation

Whole aortic valves with their aortic root were extracted from 13 fresh porcine hearts procured from a local abattoir and kept on ice during transport. The pigs were 6 months old at time of slaughter. The individual leaflets were identified and cut out at the root to be stored in 1× phosphate buffered saline (PBS) for same day testing. Leaflets were placed on a glass slide under an elliptically polarized microscope for dissection. The polarization was used to identify fiber bundle and membrane structures. Only one specimen was taken per side (left or right) of a leaflet.

The fiber bundles in the 2nd or 3rd position from the free edge were used for biomechanical testing as they have longer, less-branched segments than bundles from other positions [75]. Fiber bundles were cut to approximately 10 mm-long specimens with the whole length of the bundle intact. The specimens were sandwiched between 2 mm wide strips of paper using a fast acting adhesive which created clamp points. Once the adhesive had fixed, the specimen was immersed in PBS and was ready for testing.

The membranes between the 2nd an 3rd fiber bundles from the free edge and 5 mm from the root have the largest area free of fiber bundles (Figure 30), and were used for testing. Membrane specimens were cut radially with a transected fiber bundle on each end to serve as clamp points. Each membrane specimen was a strip 0.6 – 3 mm wide with an area in the center free of fiber bundles. The membrane specimens were then glued between paper strips identically to fiber bundles specimens for biomechanical testing.

4.2.2 Uniaxial tensile micro-testing

A uniaxial micro-tensile testing system as described in Chapter 3 was built to test the specimens having a diameter of approximately 0.5-3 mm and approximately 5-15 mm length under loads up to 25 N. The testing system was designed to fit on the stage of our custom, motorized optical microscope (BX50, Olympus Inc., Center Valley, PA). Two stainless steel clamps held the specimen in the field of view during testing. One clamp was fixed to a load cell, which output a voltage signal through a custom made differential amplifier to a data acquisition device (Labjack Inc). The other clamp was attached to a stepper motor (1.5 μm/step, NEMA 8, Haydon-Kerk Inc.). To ensure accurate synchronization, the activity of the stepper motor was monitored via an opto-isolator circuit connected to the data acquisition device. Real time video at up to 60 Hz was synchronously acquired via a digital camera (PL-A686, Pixelink, Inc.) to record specimen deformation during testing. The *x*-axis of the microscope stage was synchronized with the extension motor of the micro-testing system to maintain proper field-of-view. The system was controlled through a custom GUI programmed in Matlab (Mathworks, Inc.) and in-house programs developed in both Matlab and C.

Tensile tests were performed to stretch each specimen up to 1-3 mm tensile elongation through the 'toe' and 'linear' regions of the stress-strain curve. During the biomechanical test, samples were kept hydrated by constant drip immersion in PBS. Immediately before each test, the specimen was preconditioned with 5 cycles of 50% displacement to produce consistent stress-relaxation data [84, 85]. In each test, the specimen was stretched at a constant rate to a fixed displacement, held at that displacement for 20 seconds (initial tests held specimens over 30 seconds but there was no measurable additional relaxation after 15 seconds), and then relaxed to the original displacement. For each specimen, tensile strains were applied at two different rates: a slower rate (0.3 mm/sec) was applied for optimized video focus adjustment and acquisition at 10 Hz and a faster rate (0.75 mm/sec) was applied to quantify the loading and viscoelastic behavior. This protocol was done for 31 fiber bundle specimens and 35 membrane specimens.

4.2.3 Strain field calculation

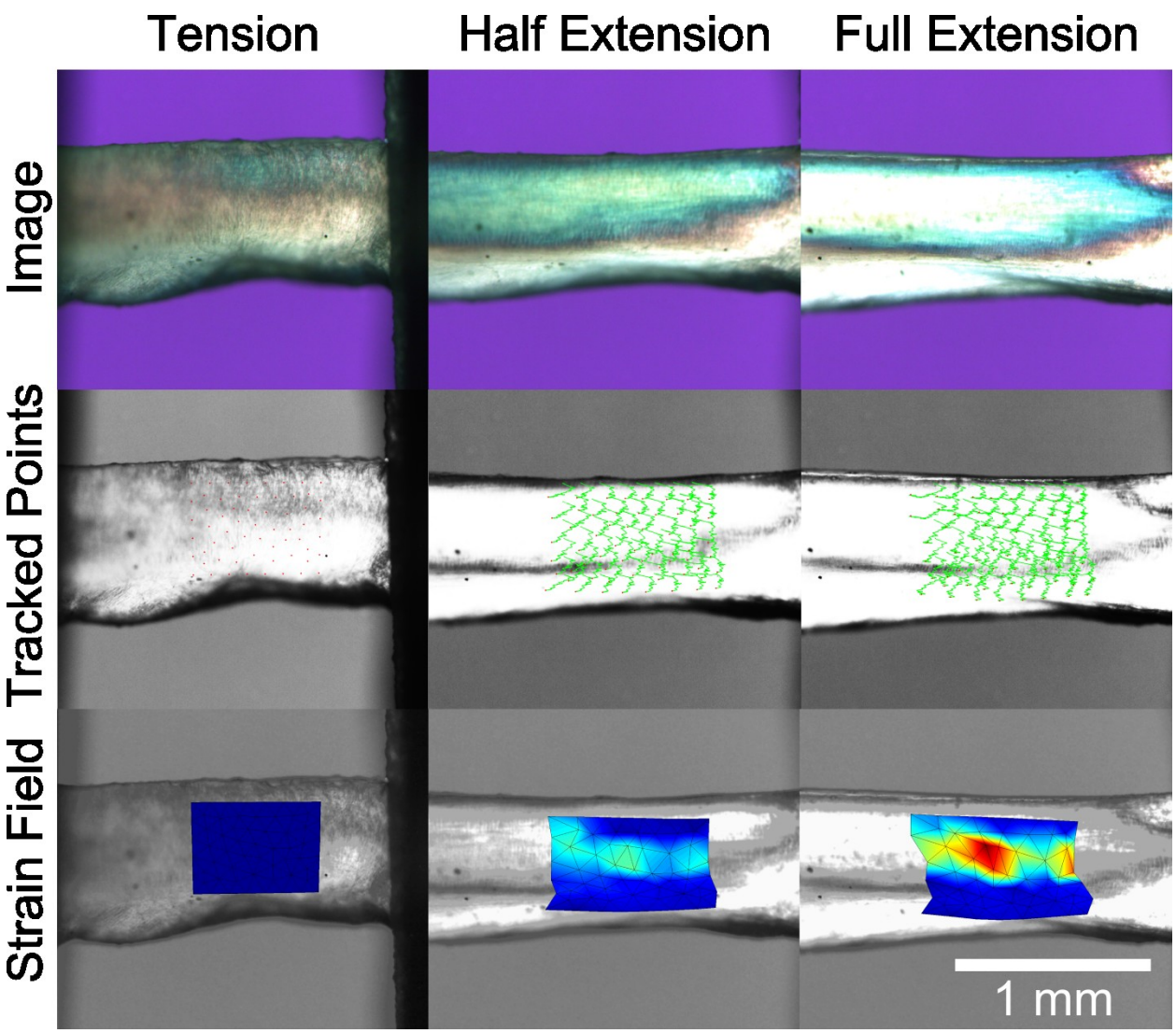

Figure 31 Optical strain-tracking of a fiber bundle specimen using polarized light. The fiber bundle changes to a bright blue as the specimen is stretched and the collagen becomes more uniformly aligned. The green lines following the tracked points indicate the path of each point through the video. In full extension, the upper fiber bundle has undergone larger strain than the surrounding tissue.

Due to non-uniform (heterogeneous) specimen deformation, specimen strain could not reliably be achieved from clamp-to-clamp displacement. Instead, strain was computed using pixel-level 'feature tracking' of synchronized video data. The video data for each specimen was separated into sequential images using the video

processing tool 'VirtualDub' (http://www.virtualdub.org). A region of the specimen in the image was populated by a 2-D triangular mesh with nodes at ~ 0.1 mm interval (Figure 31). These points were tracked via image-correlation through the sequential images using our previously developed software [74]. The measured deformations were then computed as a 2-D strain field and plotted for the duration of the test (Figure 31). The *x*-axis (in the direction of the applied displacement) and *y*-axis (perpendicular to the applied displacement) tensile strains were averaged to yield estimates of the *x*-axis and *y*-axis strain as a function of time.

4.2.4 Data analysis

A total of 31 fiber bundle and 35 membrane specimens were tested. Experimental problems such as premature failure or clamp slippage caused 19 specimens to be discarded, leaving 25 fiber bundle and 22 membrane specimens suitable for analysis. The membrane specimens consistently underwent a 'rebound' when they were cut free of the surrounding fiber bundles.

From each displacement versus force curve, five biomechanical properties were estimated: the instantaneous modulus of the linear region (E_0), the relaxation time constant (τ), the strain at the start of the linear region (ε_{lin}), the equilibrium modulus (E_∞) and the degree of relaxation ($\zeta = 1 - E_\infty/E_0$) as a relative measure of viscoelasticity. The value of E_0 was calculated via least squares linear regression of stress versus strain during loading. The τ was calculated by inverse of the linear regression of the slope of the natural logarithm of the stress data versus time immediately following the peak stress. The equilibrium modulus was the elastic modulus multiplied by the ratio of the equilibrium stress to the peak stress.

With both specimens, the zero strain was defined to be ε_{lin}. This yielded new strain values using the following formulae where α was the new zero strain point, L was the length, and λ was the stretch.

$$(1)\ \lambda(t) = \frac{L(t)}{L_0}$$

$$(2)\ \lambda'(t) = \frac{L(t)}{L_\alpha}$$

$$(3)\ L_\alpha = \lambda(\alpha) * L_0$$

$$(4)\ \lambda'(t) = \frac{L(t)}{\lambda(\alpha) * L_0}$$

$$(5)\ \lambda'(t) = \frac{\lambda(t)}{\lambda(\alpha)}$$

5-factor QLV equation:

$$(6)\ T(t) = A[\lambda(t) - 1]^B + AC \int_0^t [\lambda(t - \tau) - 1]^B$$

$$\frac{1}{\tau}\left(\frac{e^{-\tau/\tau_1} - e^{-\tau/\tau_2}}{1 + C\ln(\tau_2/\tau_1)}\right) d\tau$$

Linear elastic parameter: A

Non-linear elastic parameter: B

Viscoelastic parameters: C, τ_1, τ_2

Additionally, a representative fiber and membrane was selected for each specimen to be fit with a 5-parameter quasilinear viscoelastic (QLV) model using a direct-fit approach that had been previously applied to aortic valve tissue (Equation 6) [86]. This modeling tested the feasibility of using such an approach for future work to analyze the mesostructures' loading and relaxation behavior.

4.2.5 Statistical tests

For statistical tests, $p > 0.05$ were considered not significant. E_0, τ, ζ, and E_∞ were each compared with the following tests: a Student's *t*-test comparing the membrane and fiber bundle specimens, one way ANOVA comparing the leaflets of a particular specimen type, and Student's *t*-tests comparing the left and right sides of leaflets. Also, a Pearson's correlation coefficient, *R*, and probability of no correlation (*p-null*) were calculated between the width of a specimen and E_0, τ, ζ, and E_∞. There was also an *R* value and *p-null* calculated between the maximum specimen strain and E_0, τ, ζ, and E_∞.

4.3 Results

Overall, the fiber bundles had significantly different moduli but similar viscoelastic biomechanical properties compared to the membrane specimens. Metrics such as E_0 and τ are summarized in Table 3.

Specimen	Leaflet	Elastic Modulus (MPa)	Degree of Relaxation	Relaxation Time Constant (sec)	Equilibrium Modulus (MPa)
Bundle	Left	15.24 ± 5.03	0.260 ± 0.05	4.821 ± 1.739	10.62 ± 3.57
	Non	24.50 ± 7.02	0.248 ± 0.021	10.024 ± 2.136	18.48 ± 5.39
	Right	6.23 ± 1.22	0.202 ± 0.026	8.325 ± 1.985	4.79 ± 0.95
	Total	*13.87 ± 2.81*	*0.232 ± 0.019*	7.280 ± 1.335	*10.26 ± 2.10*
Membrane	Left	1.29 ± 0.43	0.129 ± 0.026	4.347 ± 1.137	1.13 ± 0.37
	Non	2.23 ± 0.50	0.229 ± 0.042	6.492 ± 2.484	1.80 ± 0.46
	Right	2.94 ± 0.68	0.256 ± 0.055	8.280 ± 1.143	2.25 ± 0.53
	Total	*2.27 ± 0.36*	*0.213 ± 0.029*	6.206 ± 1.01	*1.80 ± 0.29*

Table 3 Averaged values of E_0, τ, ζ, and E_∞ (± SE) of each leaflet for each specimen type.

4.3.1 Video data

Imaging results showed that as the membrane specimens were stretched, the initially crimped fibers became straightened along the direction of loading. The fiber bundles also tended to rotate and become oriented during extension. Neither specimen type showed any reorientation during the hold phase of the tests. The strain perpendicular to the displacement (*y*-axis) increased in both specimens. The ratio of perpendicular strain to parallel strain was not significantly different between specimen types (membrane 0.27 ± 0.12, bundle 0.46 ± 0.12, $p > 0.05$).

4.3.2 Loading data results

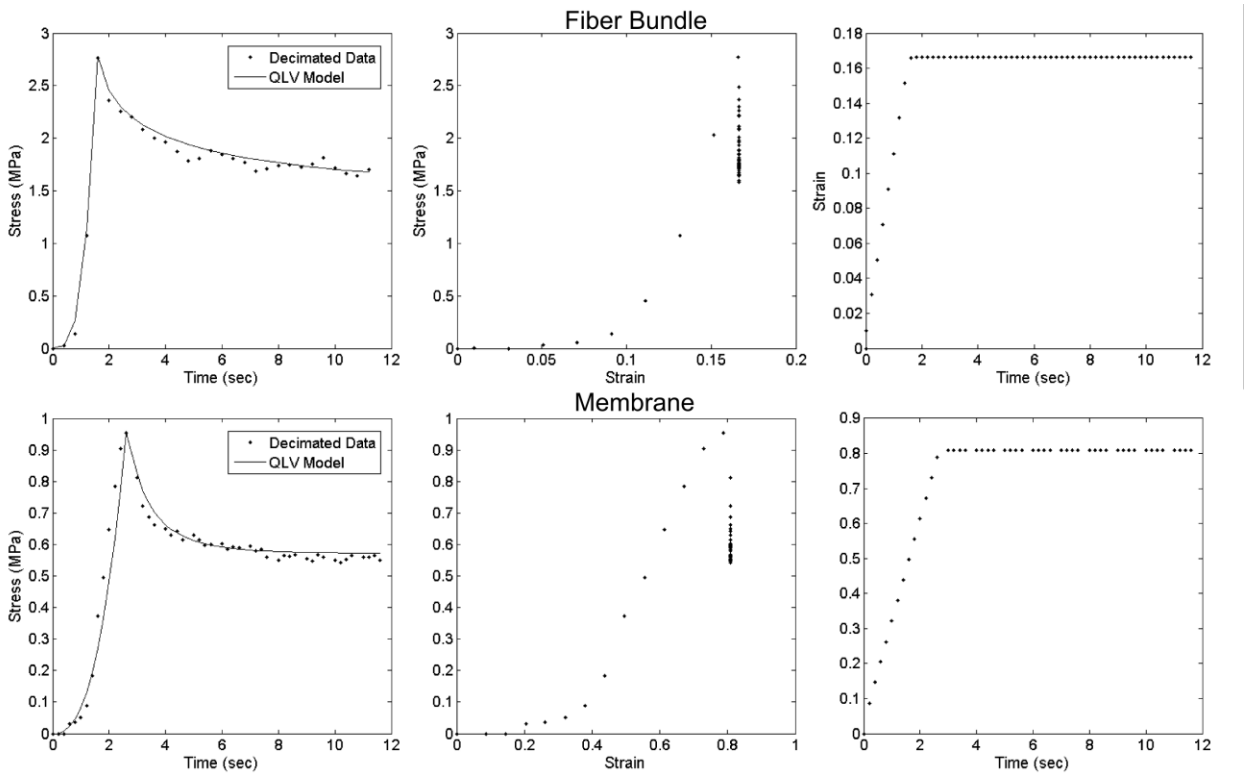

Figure 32 Representative stress-time, stress-strain, and strain-time curves for a fiber bundle and membrane specimen depicting the first 12 seconds. A QLV model has been fitted to the stress-time data. Both the fiber bundles and the membrane show a toe region, followed by a linear region, and a relaxation in their stress curves. The peak stress for the fiber bundles was consistently higher. Frequently, there was a more significant strain required to stretch the membrane specimen into the linear region of loading.

Representative stress-time, stress-strain, and strain-time data with QLV model curve fits are shown in Figure 32. The resulting curves have typical soft tissue toe region and linear region during loading, followed by relaxation during the holding period. The mean E_0 was significantly higher for the fiber bundles compared to the membrane structures (p <0.001, Figure 33A). When comparing the heterogeneity associated with samples from different leaflets, we found significant variation of fiber bundle E_0 between the leaflet locations. Those from non-coronary and left coronary leaflets had the higher E_0 than from the right leaflet (p <0.05, Figure 33B). However, we did not find significant differences between the membrane samples of different leaflets (Figure 33C).

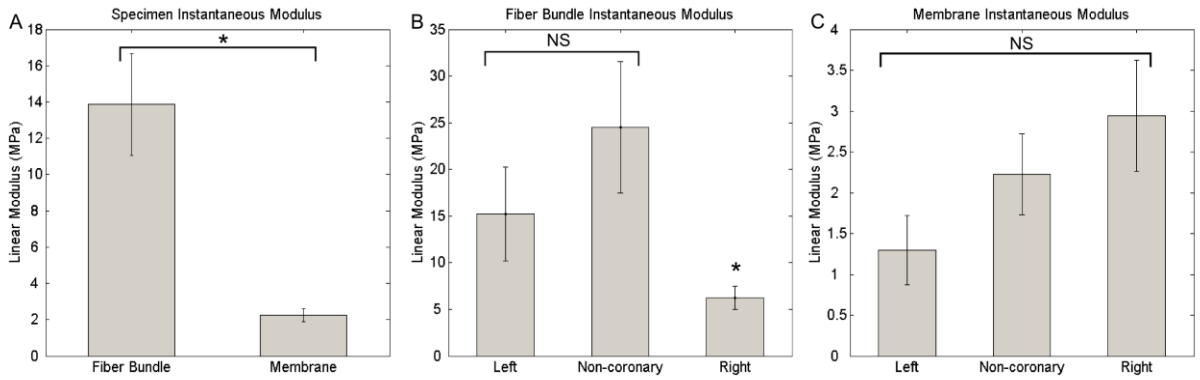

Figure 33 Comparison of the instantaneous linear modulus between specimens and leaflets. * indicates p <0.05. Error bars indicate standard error.

Membranes and fiber bundles had similar degrees of relaxation, ζ (0.223 ± 0.016), and relaxation time constant, τ (6.75 ± 0.73 sec). The width of the fiber bundle specimens negatively correlated with the E_0 (R = -0.47 ± 0.32, p <0.02) and E_∞ (R = -0.50 ± 0.31, p <0.02). There was no significant correlation between the membrane width and any of the observed metrics nor was there a significant correlation between the fiber bundle width and τ or ζ. We did find a significant negative correlation (R = -0.52, *p-null* <0.02) between max strain and E_0. However, as every specimen was stretched till it reached the linear region of its loading curve, this trend is an artifact of our methods; a less rigid membrane specimen would likely have to be stretched further to get the linear region its stress-strain curve.

The preliminary QLV model fits were achieved with *A, B non-linear elastic* and viscoelastic (C, τ_1, and τ_2) parameters estimated for representative fiber bundle and membrane specimens (Equation 6). The parameters converged to: $A = 6.59*10^9$Pa, B = 4.08, C = 0.238, τ_1 = 0.006s, τ_2 = 20s for the fiber bundle and $A = 6.8*10^6$Pa, B = 3, C = 0.75, $\tau_1 = 4.6*10^{-4}$s, τ_2 = 2s for the membrane.

4.4 Discussion

4.4.1 Elastic biomechanical properties of fiber bundles and membranes

In this study, we quantified the biomechanical properties of two major matrix constituents of porcine aortic valves, the fiber bundles and membranes. Overall, the fiber bundles were shown to have significantly higher instantaneous and equilibrium tensile moduli than the membranes (Figure 5A). These variations are correlated with their distinctive structural features. Within each fiber bundle, the collagen fibers are densely packed and mostly aligned along the longitudinal direction of the bundle. In comparison, the membranes are mostly composed of multi-oriented fibers in the transverse directions. The higher degree of collagen alignment thus contributes to the higher tensile moduli along the bundle longitudinal axis. Having the collagen fibrils organized into a fiber bundle could increase the crosslinking which also can increase the stiffness [87]. In each leaflet, the fiber bundles are aligned circumferentially (Figure 1). As a result, each leaflet is characterized with highly anisotropic tissue-level biomechanical properties, as reported previously (28 ± 10 MPa circumferentially, 1.33 ± 0.42 MPa radially in porcine aortic leaflets) [66]. The fiber bundles are possibly the dominate load bearing component that contributes to the circumferential tensile stiffness *in vivo* and aides in the distribution of stress [26, 88].

A negative correlation was observed between the fiber bundle width and E_0 and E_∞. A similar trend was reported by Legerlotz et al in tendon fascicles where cross sectional area negatively correlated with strain and elastic modulus [89]. They suggested that this could be a result of larger bundles having less uniform alignment in their constitutive fibrils.

While the tensile modulus of membranes was found to be significantly lower, the membranes also play critical biomechanical roles for the leaflet function. They are highly distensible as evidenced by their significant collapse when cut free of the fiber bundles. These thinner regions of the leaflet likely give the leaflet increased flexibility allowing the valve to rapidly open and close during systole and diastole, respectively [59]. These thinner regions are also where the fibrosa layer would be more capable of folding and undergoing compression during systole [32].

4.4.2 Relaxation Behavior

The relaxation behaviors observed in the fiber bundle and membrane specimens showed similar degrees of relaxation and relaxation time constants. These results suggested that the interactions between the fibrils of the fiber bundle likely did not induce different relaxation behaviors when compared to the more widely distributed fibrils of the membrane.

This observation contrasts with the previous study by Stella et al, which reported different relaxation percentiles in the radial (33.28 ± 1.35%) and circumferential (27.51 ± 1.07%) directions. Both these values are significantly higher than the degree of relaxation observed in our membrane and fiber bundle trials. This difference may be due to the location of the specimens. Stella et al's specimens were taken from the lower belly of the leaflet. This region of the leaflet has different fiber bundle morphology with different stress and elastic moduli than the near-coapting region from which this study's specimens were extracted [31, 75].

Heart valve relaxation has been usually characterized by fast (<1 sec) and a slow (>100 sec) time constants with the latter being more influential at high strains [79, 90]. As the specimens in this study were stretched into the start of the linear region we decided to characterize the overall relaxation using a single time constant. Shen et al tested the viscoelastic properties of isolated collagen fibrils and found a fast time response of 7 ± 2 sec and a slow time response of 102 ± 5 sec [91]. This fast time constant is close to the membrane and fiber bundle relaxation time constant results from our study, which further suggests the mechanism of relaxation behavior functions in large part at the fibril level scale.

An alternative explanation may be result of fact the membrane structures required additional stretching to get into the linear region. This may have pulled the collagen fibers far enough that there was little room for relaxation as the majority of the fibrils had been recruited. This space for the collagen to realign had been suggested by Dr. Vesely as an explanation for the directional differences in the relaxation properties of the ventricularis [32]. Dr. Anssari-Benam's thesis demonstrated that the degree of relaxation decreased and relaxation time increased in aortic valve specimens as the strain approach the failure strain [38]. This may influence the results because of the additional displacement required in the membrane specimens. The net effect could be a reduction in their degree of

relaxation and an increase in their relaxation time. This shift may have played a role in producing no significant difference in the degree of relaxation and relaxation time constant relative to the fiber bundles. Verification of this would require testing the specimens at multiple strain levels and stretching them to failure. It is worth noting that our degree of relaxation values were within the ranges Dr. Anssari-Benam observed [38].

4.4.3 Variability between heart valve leaflets

Here, for the fiber bundle, the leaflet-associated variation is $E_{non\text{-}coronary} > E_{left} >> E_{right}$ (Figure 33). This heterogeneity between the fiber bundles is likely a modification for different loading conditions and functions between the aortic valve leaflets. We found no consistent differences in the width of the fiber bundles used in this study between the leaflets, suggesting that this trend is independent of the observed negative correlation between fiber bundle width and elastic modulus. Grand et al reported that, in human aortic valves, the non-coronary leaflet has the greatest stress and elastic modulus followed by the right coronary leaflet and the left coronary leaflet [31]. They suggested the presence of a coronary ostium may relieve the diastolic pressure in the right coronary and left coronary leaflets. Higher systolic pressure could result in greater stress in the non-coronary leaflet, thus leading to structural remodeling/adaptations. Our previous work had identified differences in fiber bundle morphology between leaflets which could be related to different biomechanical behavior [75]. In particular, the non-coronary and left coronary leaflets had consistent asymmetric fiber bundle arrangement compared to the right coronary leaflet. Our current study suggests that the leaflets adapt at the fiber bundle level for different loading conditions.

We did not observe significant variations in the biomechanical properties of membranes between the leaflets. The membrane appears as a less oriented material with only small, non-significant thickness variability between the leaflets. As the major stress is likely supported by the fiber bundles, we speculate that the variability in loading conditions across the leaflets would have less of an impact on the biomechanical requirements of the membrane. Instead, the difference in loading conditions may produce different the ratios of membrane area to fiber bundle area in regions of a leaflet and across leaflets.

Balachandran et al reported how the degree of cyclic stretch influenced cell proliferation, apoptosis and enzyme expression as a mechanism for collagen remodeling. These variables were comparable to fresh controls at 10%

cyclic strain, enhanced at 15% cyclic strain, and started to decrease at 20% cyclic strain [92]. This mechanism could be the root cause of the localized variability in the membrane and fiber bundle biomechanical properties by encouraging reinforcement in the high strain areas. However, because the fibrils of the fiber bundle are tightly packed, the fiber bundles may be less responsive to this mechanism relative to the membrane after initial formation.

4.4.4 Polarized-light assisted strain tracking

This study is the first to report results of valve mesostructure properties using a newly designed micro-testing and imaging system. An advantage of this system over those commercially available is the ability to acquire elliptically polarized video/images during the uniaxial tensile tests *with synchronized stage and actuator displacement*; thus keeping the specimen within the microscope field-of-view during testing. Calculation of strain fields using image correlation could then be done which is likely better than calculating displacement/strain from the grips or edge of the specimen. Furthermore, this instrument enabled direct visualization of morphological details and specimen rearrangements during stretch. With the aid of polarized light, the images showed clear rearrangement of the constitutive fibrils as they uncrimp and become more aligned during stretch as we have previously observed [75]. Eventually, most of the fiber bundles rotated into the direction of loading (in the 'toe-region') with subsequent linear increase in stress-strain behavior. As there were no visibly detected changes in deformation during relaxation, the relaxation behavior is more likely an intrinsic property of the collagen protein and fluid transport rather than a product of reorientation of the fibers. This system could likely be applied to other soft tissue micromechanical testing such as for tendons, ligaments, and fascia tissues.

4.4.5 Limitations

All care was taken to minimize specimen damage during dissection, but clamping was difficult for these small specimens. Due to clamping challenges, the membrane specimens were only tested in the radial direction. In addition, fiber bundles tend to branch, widen and overlap towards the root/belly (see Figure 30). Thus for this study fiber bundle specimens were taken closer to the free edge where bundles are more defined.

Preliminary analyses using the direct-fit method (5-parameter QLV model) were achieved for each mesostructure (Figure 32), but further work will be needed detailed quantification of the mesostructures' non-linear

loading and relaxation behaviors. With a sufficiently larger data set, trends between left and right sides of leaflets and further non-linear properties can be identified.

4.5 Conclusion

This study presents, to our knowledge, the first data quantifying the differential biomechanical properties of fiber and membrane *mesostructures* of aortic valve leaflets. These data may be useful not only for basic understanding of the valve, but also for analyzing and developing improved strategies for replacement/repair and designs of novel tissue-engineered constructs.

Chapter 5: Conclusions and Future Directions

The fundamental questions of this thesis were what mechanisms would encourage the formation of the fiber bundle and membrane mesostructures and what possible adaptive advantage arises from this heterogeneous configuration and asymmetry. It has been well established that the aortic valve leaflet has different elastic and viscoelastic properties in the radial versus circumferential directions. However, as the previous studies typically did not delineate between the fiber bundles and the membrane, we could not to determine if those trends were a product of the overall arrangement or the specific contribution of one or more of the substructures. For example, in Dreissen et al's 2005 study on the collagen fiber alignment, they suggested that the variability observed in the collagen alignment could be a result of two distinct populations of differently aligned collagen fibers [67]. This trend could be readily be explained by one population being the fiber bundle and the other the membrane mesostructures.

5.1 Important Findings

1. There is significant morphological variability in fiber bundle organization through the regions of an aortic valve leaflet and between different leaflets.

The literature suggested adopting the perspective that the fiber bundles exist as projections of the aortic root which are anchoring into the underlying membrane and reinforcing it. The functional role of these fiber bundles would be to allow the load to be readily transferred from the leaflet to the aortic root [68]. However, in light of this and other recent work, we cannot continue the previous representations of fibers bundles as uniform, continuous packages of collagen fibrils that run from side to side of the leaflet. In this thesis, we identified many several distinct branching patterns showing how the fiber bundles interface with the underlying membrane as well as the overarching trends in how they are organized in the leaflets. Each of the branching patterns may play an important role in how load is gathered throughout the aortic valve leaflet. These patterns were regionally specific, having different patterns dominant in the belly, root, coapting region, and free edge. This heterogeneity is very likely an adaptation for the different stress and strains of each region that has been reported [31, 93]. Along with the variability in fiber bundle diameter and the spacing between the fiber bundles, these branching patterns could account for the regional variability in leaflet stiffness. The branching of the leaflets likely aid both the flexion of the

fibrosa layer as well as flattening the leaflets in the coapting regions [34]. This could be evaluated with a mathematical model comparing leaflets with dispersed versus tightly collected fiber bundles.

The organization of the fiber bundles varies across the leaflets between relatively symmetry and significant asymmetry. An asymmetric design would organize the overlap in the fiber bundles embedded in the aortic wall which in turn would manage the stress transferred to a single region of the aortic wall. It is possible that the fiber bundles run continuously along the aortic root from leaflet to leaflet or they intermesh with the aortic sinus. Additionally, these asymmetries may create points along the free edge where the valve would readily open given Marom et al's model found asymmetric leaflets opened more rapidly and underwent greater during systole relative to symmetric leaflets [52]. Evaluation of these hypothesizes would require imaging the fiber bundles of the leaflet and then following them through an intact aortic root. The whole leaflet evaluation of fiber bundle arrangement was directly building on the studies done by Dr. Doehring that characterized the leaflet asymmetry in terms of fiber bundle diameter and distribution [59]. The findings in this thesis consistently agreed with the trends reported by Dr. Doehring's though this study observed a significantly lower mean fiber bundle diameter. This could have been attributed to the improvements in the imaging technique making it easier to delineate the fiber bundles from the membrane structures.

2. The fiber bundle and membrane substructures have significantly different elastic properties but similar viscoelastic properties.

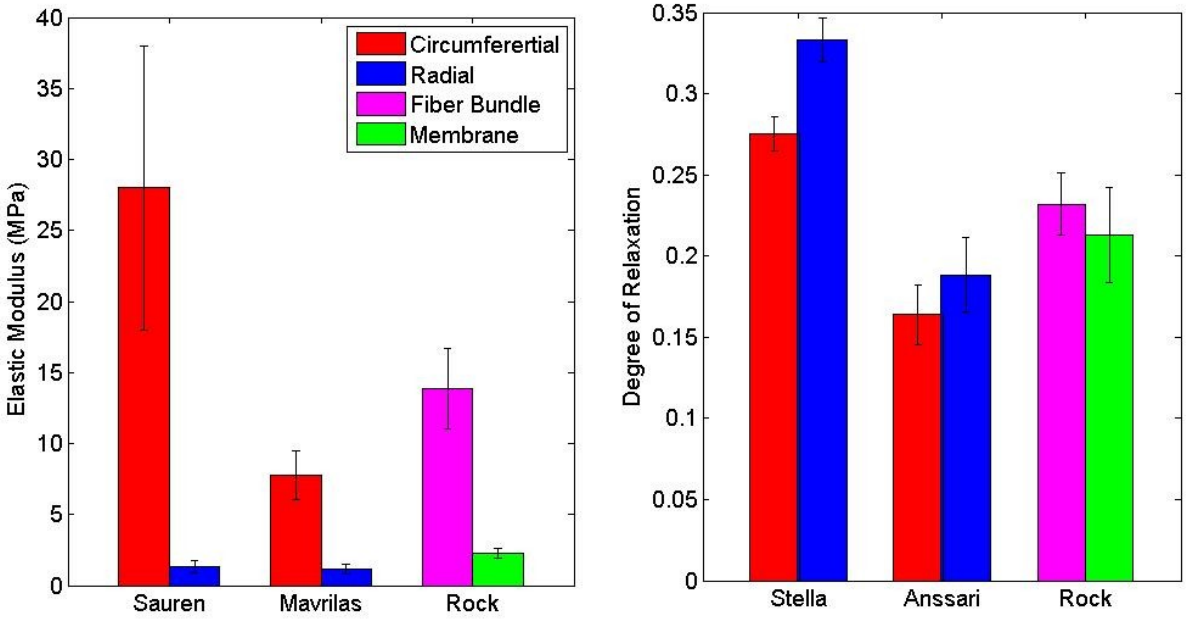

Figure 34 Bar graphs comparing previous estimates of elastic modulus and degree of relaxation in the circumferential and radial directions to that of the fiber bundle and membrane specimens in this thesis (Sources: Sauren 1983, Mavrilas 1991, Stella 2007, Anssari-Benam 2011).

We observed an order of magnitude greater elastic modulus in fiber bundles relative to membrane structures. This trend was consistent with the previous studies of significantly larger circumferential stiffness relative to radial stiffness in whole leaflets and the layers of the leaflet (Figure 34). Compared to the previous studies, the relative difference in the elastic modulus between the mesostructures was not as severe as the difference between the directions of intact leaflets. Most likely, the radial loading behavior is a result of the collagen fiber bundles being realigned rather than a property of the membrane given fiber bundles required additional elongation to be loaded. This degree of stretch may not have occurred in the previous radial testing which may account for the discrepancy. While it has been largely assumed that the fiber bundles are the major load-bearing structure, this thesis directly evaluated and confirmed that assumption. This idea is reinforced by the fact the membranes would tend to collapse down upon being cut free of the surrounding fiber bundles.

The membrane and fiber bundles showed similar relaxation behaviors with an insignificant difference between their relaxation time constant and degrees of relaxation. As the fiber bundle specimens can be viewed as circumferential specimens and the membrane specimens were cut radially, this is a direct contrast to previous studies that observed significant effects of directionality on leaflet relaxation (Figure 34) [37, 38]. The relaxation behavior of the leaflets was suggested by Sacks et al to be a combination of factors at the tissue and fibril levels such as fibril slipping and the proteoglycans [8]. An alternative theory is that relaxation occurs by the collagen realigning and thus is more pronounced in areas where the collagen has a greater capacity to shift which would explain the directional variability observed [30]. This should have produced greater relaxation in the membrane specimens as they have lower collagen fibril density so more capacity to relax. However, as mentioned previously, given the difference in elastic moduli between the mesostructures and degree of stretch required for loading, it is more likely that the intact tissue radial relaxation is in fact mostly governed by the fiber bundles as they have a greater contribution to the load bearing. This would suggest the leaflet reorients the fiber bundles to the point of the fiber bundles being stretched radially. Thus, the radial behavior previously noted would likely be a product of the fiber bundles being bent and twisting instead of the membrane structure. The viscoelastic properties observed in this thesis had values to be similar to that of isolated collagen fibrils. This suggested that the relaxation behavior operates at the fibril scale with a mechanism such as the fibrils sliding along one another for both substructures. We did acknowledge that the degree of relaxation as well as the relaxation time constant of the membrane could be influenced by the greater displacement applied in the biomechanical tests relative to the fiber bundle specimens. This could stretch the membrane structures to the point of fully aligning the fiber bundles and leaving little room for reorientation that may produce greater relaxation at lower strains.

Another significant factor to the loading and relaxation behaviors could be the interface point between the fiber bundles and membrane structures. Evaluating the biomechanical interactions between the membrane and fiber bundles would require an additional study on regions of intact leaflets that then have the structures isolated for comparison. We hypothesize that this would be very regionally specific given the regional heterogeneity in fiber bundle composition and branching patterns.

3. The fiber bundles of different aortic valve leaflets have significantly different elastic properties.

Previous studies had established that the mechanical properties of the aortic valve leaflets and sinuses vary between the three leaflets [12, 31, 52]. The suggested factors driving of such configurations were different hemodynamic pressures or variability in the amount of strain to maintain coaptation due to either leaflet size or symmetry. However, the previous works were limited in their ability to offer a direct mechanism behind the observed variability in leaflet stiffness beyond density and alignment of the collagen fiber bundles. Balachandran et al had established that the degrees of cyclic strain can influence the collagen synthesis in the leaflet which could account in part for the difference in leaflet stiffness [92]. This thesis suggests that the biomechanical adaptations go beyond the overall morphology and arrangements of the fiber bundles. Rather, the valve has adaptations on the scale of the individual fiber bundles that may facilitate the overall organ function. As the fiber bundles extend into the aortic root, the variability in fiber bundle stiffness between the leaflets could not only offer an explanation as to the variability in the leaflets' mechanical properties but also the variability of the aortic sinuses. As the size of the fiber bundles was dismissed as a cause of trend between the leaflets, the mechanism for the leaflet variability in fiber bundle elastic modulus is unknown though likely factors are constitutive fibril diameter, alignment and density.

5.2 Contributions to the Field

The heart valves require both rigidity and flexibility of their leaflets to regulate the flow of blood in and out of the heart. The hierarchy of collagen fiber bundles and membrane that comprise the aortic heart halve leaflet rose as an evolutionary advantage of that design to meet that need. This thesis was the first to give a detailed characterization as to how these structures are organized in the aortic valve. Also, exactly how the fiber bundles and membranes each contribute to the net mechanical behavior of the valve has been explored and quantified for the first time in this thesis. This knowledge will facilitate replacement valve designs, particularly tissue engineered constructs, to mimic the behavior of the native tissue to improve replacement lifespan and efficacy.

Additionally, there is the technical contribution of the testing system. This novel, custom system allowed us to acquire centered, in-focus video data during uniaxial displacement tests. This revealed the changes in the collagen fibrils during loading as well as permitting optical tracking to quantify local strain fields. Without these, there would

be significant gaps in the data forcing simplifications that could compromise the results published in this thesis. This testing system could be readily adapted for a variety of small-scale soft tissue testing.

5.3 Future Directions

5.3.1 Develop a new computational model based on mesostructures' biomechanical properties

The next step in analyzing the role of the fiber bundle and membrane mesostructures in aortic valve function is to develop a model that incorporates the morphological and biomechanical characteristics of each substructure representing aspects of the non-affine deformation and stress-strain behavior of the heart valve leaflet during its functional cycle. We hypothesize that a structurally based computational model will better represent the bending and shear mechanical behavior of native valves than a standard finite element model that treats the leaflet as a homogeneous material. As the fiber bundles tend to run circumferential, the mechanical behavior of the valve tissue as a whole is likely to be similar to the fiber bundles in the circumferential direction and the membrane region in the radial direction. To acquire the loading cycle data to represent, one could use larger specimens of heart valve tissue and stretch them in the circumferential as well as the radial directions at loading rates similar those in Chapter 4. Then, two finite element models will be created. The first model will use a continuum approach similar to those seen in the literature. The second model will be a combination of fiber bundles and membranes representing the tissue as its mesostructure's organization.

We expect that membranes can be treated like a 2 dimensional mesh and the fiber bundles like viscoelastic springs. Our lab has made previous use of the FEA software package Tochnog (website: http://tochnog.sourceforge.net/) in modeling the deformations of Achilles' tendon collagen fascicles. The membrane will be represented as a 2 dimensional mesh and the fiber bundles as viscoelastic cylinders or beams that are embedded within it. The arrangement of the bundles will be derived from polarized light images of leaflet specimens such as those from Chapter 2. This model may look to incorporate other model's representation of the change in fiber orientation[60].

Once both models are established, we will then look to compare their ability to predict the stress-strain of the whole tissue. The non-continuum approach allows for non-affine deformation which should yield a more accurate representation of the whole tissue's behavior.

Alternative modeling methods approaches include, a beam and cable finite element model, representing the fiber bundles as leaf springs, or the entire leaflet as a fiber-reinforced composite material[49]. If there is very significant sliding of the fiber bundles along the membrane, a more complicated model involving a frictional equation between the membrane and fiber bundles may be required.

5.3.2 Scanning and testing human aortic valves

There are several significant differences between human and porcine aortic valves. This is a product of both the difference size of the two species as well as the fact pigs are quadrupeds which produces different gravitational forces on aortic blood flow [94]. The relative difficulty of procuring non-diseased human aortic valve specimens necessitated working with porcine aortic valves for the initial work with this testing system. With this work as a proof of concept for the methods and test system, it is now possible to pursue testing human aortic valve specimens. By determining differences in morphology and biomechanics of human versus porcine aortic valve mesostructures, we could identify species-specific adaptations that have been made to the tissue. This could prove invaluable in developing a tissue-engineered valve tailored for the eventual end-user species, humans.

5.3.3 Characterize toe region biomechanical behavior with a more thorough QLV approximation

Although additional stretch was required to extend the membrane specimens, we were unable to find a statistically significant different in the length of the toe region between the mesostructures. This was in part as the focus of these trials was to quantify the linear region of the specimens. Additionally, it was difficult to establish where loading started given the significant relaxation of the membrane specimens when cut free of the surrounding fiber bundles. To that end, a follow-up study performing repeated measurements and longer relaxation times (~1000s) could produce data capable of being analyzed with the revised QLV function. This in turn, could be used to refine the mathematical model by determining how much stretch occurs before loading and before the linear region of the stress-strain curve.

5.3.4 Evaluate left-right side biomechanical asymmetry

From our work presented in Chapter 2, we know there is significant morphological asymmetry in the non-coronary and left coronary aortic valve leaflets. The sample size of this study and the large specimen-to-specimen variance prohibited us from drawing any significant conclusions about any variability observed in the biomechanical properties of the mesostructures between sides of a leaflet. A larger data set may reveal different biomechanical adaptations at the mesostructure scale for asymmetric loading between the sides of the leaflet.

5.3.5 Explore the role of elastin and compare mesostructure molecular composition

We attributed the difference in biomechanical properties of the fiber bundles and membrane substructures to the more uniform organization of the collagen fibers in the fiber bundles. However, it is possible that these trends are also produced by the presence of elastin fibers as well as their molecular composition, namely their relative collagen and elastic content. Elastin is not naturally birefringent so it would require a refinement of the protocols used in this thesis such as the introduction of stains or treating the leaflets with a collagenase. A chemical assay of the mesostructures would allow us another perspective by which to analyze the substructures and interpret the differences in their biomechanical properties. A significantly higher elastic content in the membrane structure would further support the idea that the membrane serves as a flexible component of the valve leaflet.

5.3.6 Apply testing system to other soft tissues

In addition to testing human aortic valve tissue, there are a number of soft tissues with structures that operate on the fiber bundle scale such as tendons, ligaments, aortic sinuses, and the other valves of the heart. This system could be readily adapted to test such soft tissue specimens. In particular, my colleague Dr. Olusenni Komolafe discussed employing such a system to test individual tendon fiber bundles [95]. As mentioned at the start of Chapter 3, one of the biggest obstacles to testing soft tissue at this scale is the development of a reliable testing system that can quantify both load data, have displacement control, and quantify non-affine strain while collecting video of the collagen reorientation.

5.4 Closing Remarks

The aortic valve's structure and biomechanical properties clearly have an environmental aspect to their creation; no two valves were close to being identical. However, despite the variance from valve to valve, there were points of convergence highlighting consistent patterns in organization and loading behavior. These are not products of chance but rather adaptations of the native tissue as part of its structure-function relationship. As we continue to establish how each of these findings contributes to the overall organ operation, we can use them to refine our mathematical models and tissues engineered designs and eventually meet the goal of an effective tissue-engineered replacement valve.

List of References

1. Freeman RV, Otto CM. Spectrum of calcific aortic valve disease: pathogenesis, disease progression, and treatment strategies. Circulation. 2005 Jun 21;111(24):3316-26.

2. Writing Group M, Roger VrL, Go AS, Lloyd-Jones DM, Benjamin EJ, Berry JD, et al. Heart Disease and Stroke Statistics 2012 Update. Circulation. 2012 January 3, 2012;125(1):e2-e220.

3. Christie GW, Barratt-Boyes BG. Age-dependent changes in the radial stretch of human aortic valve leaflets determined by biaxial testing. Ann Thorac Surg. 1995 Aug;60(2 Suppl):S156-8; discussion S9.

4. Neuenschwander S, P. Hoerstrup S. Heart valve tissue engineering. Transplant Immunology. 2004;12(3â€“4):359-65.

5. Dohmen P, editor. Tissue engineered aortic valve. HSR Proceedings in Intensive Care and Cardiovascular Anesthesia 2012; 2012; Freiburg, Germany. 2012.

6. Zimmermann WH, Eschenhagen T. Tissue engineering of aortic heart valves. Cardiovasc Res. 2003 Dec 1;60(3):460-2.

7. Misfeld M, Sievers HH. Heart valve macro- and microstructure. Philos Trans R Soc Lond B Biol Sci. 2007 Aug 29;362(1484):1421-36.

8. Sacks MS, David Merryman W, Schmidt DE. On the biomechanics of heart valve function. J Biomech. 2009 Aug 25;42(12):1804-24.

9. Butcher JT, Mahler GJ, Hockaday LA. Aortic valve disease and treatment: the need for naturally engineered solutions. Adv Drug Deliv Rev. 2011 Apr 30;63(4-5):242-68.

10. Gross L, Kugel MA. Topographic Anatomy and Histology of the Valves in the Human Heart. Am J Pathol. 1931 Sep;7(5):445-74 7.

11. Balguid A, Driessen NJ, Mol A, Schmitz JP, Verheyen F, Bouten CV, et al. Stress related collagen ultrastructure in human aortic valves--implications for tissue engineering. J Biomech. 2008 Aug 28;41(12):2612-7.

12. Gundiah N, Kam K, Matthews PB, Guccione J, Dwyer HA, Saloner D, et al. Asymmetric mechanical properties of porcine aortic sinuses. Ann Thorac Surg. 2008 May;85(5):1631-8.

13. Khan Z, Boughner DR, Lacefield JC. Anisotropy of high-frequency integrated backscatter from aortic valve cusps. Ultrasound Med Biol. 2008 Sep;34(9):1504-12.

14. Sim EK, Muskawad S, Lim CS, Yeo JH, Lim KH, Grignani RT, et al. Comparison of human and porcine aortic valves. Clin Anat. 2003 May;16(3):193-6.

15. Jamieson WR, Riess FC, Raudkivi PJ, Metras J, Busse EF, Goldstein J, et al. Medtronic Mosaic porcine bioprosthesis: assessment of 12-year performance. J Thorac Cardiovasc Surg. 2011 Aug;142(2):302-7 e2.

16. Marchand MA, Aupart MR, Norton R, Goldsmith IR, Pelletier LC, Pellerin M, et al. Fifteen-year experience with the mitral Carpentier-Edwards PERIMOUNT pericardial bioprosthesis. Ann Thorac Surg. 2001 May;71(5 Suppl):S236-9.

17. Schoen FJ, Levy RJ. Calcification of tissue heart valve substitutes: progress toward understanding and prevention. Ann Thorac Surg. 2005 Mar;79(3):1072-80.

18. Svennevig JL, Abdelnoor M, Nitter-Hauge S. Twenty-five-year experience with the Medtronic-Hall valve prosthesis in the aortic position: a follow-up cohort study of 816 consecutive patients. Circulation. 2007 Oct 16;116(16):1795-800.

19. Dijkman PE, Driessen-Mol A, Frese L, Hoerstrup SP, Baaijens FP. Decellularized homologous tissue-engineered heart valves as off-the-shelf alternatives to xeno- and homografts. Biomaterials. 2012 Jun;33(18):4545-54.

20. Baraki H, Tudorache I, Braun M, Hoffler K, Gorler A, Lichtenberg A, et al. Orthotopic replacement of the aortic valve with decellularized allograft in a sheep model. Biomaterials. 2009 Oct;30(31):6240-6.

21. Liao J, Joyce EM, Sacks MS. Effects of decellularization on the mechanical and structural properties of the porcine aortic valve leaflet. Biomaterials. 2008 Mar;29(8):1065-74.

22. Gerson CJ, Elkins RC, Goldstein S, Heacox AE. Structural integrity of collagen and elastin in SynerGraft(R) decellularized-cryopreserved human heart valves. Cryobiology. 2012 Feb;64(1):33-42.

23. Amoroso NJ, D'Amore A, Hong Y, Rivera CP, Sacks MS, Wagner WR. Microstructural manipulation of electrospun scaffolds for specific bending stiffness for heart valve tissue engineering. Acta Biomater. 2012 Dec;8(12):4268-77.

24. Argento G, Simonet M, Oomens CW, Baaijens FP. Multi-scale mechanical characterization of scaffolds for heart valve tissue engineering. J Biomech. 2012 Nov 15;45(16):2893-8.

25. Driessen NJB, Mol A, Bouten CVC, Baaijens FPT. Modeling the mechanics of tissue-engineered human heart valve leaflets. Journal of Biomechanics. 2007;40(2):325-34.

26. De Hart J, Cacciola G, Schreurs PJ, Peters GW. A three-dimensional analysis of a fibre-reinforced aortic valve prosthesis. J Biomech. 1998 Jul;31(7):629-38.

27. Driessen-Mol A, Emmert MY, Dijkman PE, Frese L, Sanders B, Weber B, et al. Transcatheter implantation of homologous "off-the-shelf" tissue-engineered heart valves with self-repair capacity: long-term functionality and rapid in vivo remodeling in sheep. J Am Coll Cardiol. 2014 Apr 8;63(13):1320-9.

28. Weinberg EJ, Shahmirzadi D, Mofrad MR. On the multiscale modeling of heart valve biomechanics in health and disease. Biomech Model Mechanobiol. 2010 Aug;9(4):373-87.

29. Clark RE. Stress-strain characteristics of fresh and frozen human aortic and mitral leaflets and chordae tendineae. Implications for clinical use. J Thorac Cardiovasc Surg. 1973 Aug;66(2):202-8.

30. Sauren AA, van Hout MC, van Steenhoven AA, Veldpaus FE, Janssen JD. The mechanical properties of porcine aortic valve tissues. J Biomech. 1983;16(5):327-37.

31. Grande KJ, Cochran RP, Reinhall PG, Kunzelman KS. Stress variations in the human aortic root and valve: the role of anatomic asymmetry. Ann Biomed Eng. 1998 Jul-Aug;26(4):534-45.

32. Vesely I, Noseworthy R. Micromechanics of the fibrosa and the ventricularis in aortic valve leaflets. J Biomech. 1992 Jan;25(1):101-13.

33. Lee JM, Courtman DW, Boughner DR. The glutaraldehyde-stabilized porcine aortic valve xenograft. I. Tensile viscoelastic properties of the fresh leaflet material. J Biomed Mater Res. 1984 Jan;18(1):61-77.

34. Vesely I, Gonzalez-Lavin L, Graf D, Boughner D. Mechanical testing of cryopreserved aortic allografts. Comparison with xenografts and fresh tissue. J Thorac Cardiovasc Surg. 1990 Jan;99(1):119-23.

35. Stella JA, Sacks MS. On the biaxial mechanical properties of the layers of the aortic valve leaflet. J Biomech Eng. 2007 Oct;129(5):757-66.

36. Sacks MS, Yoganathan AP. Heart valve function: a biomechanical perspective. Philos Trans R Soc Lond B Biol Sci. 2007 Aug 29;362(1484):1369-91.

37. Stella JA, Liao J, Sacks MS. Time-dependent biaxial mechanical behavior of the aortic heart valve leaflet. J Biomech. 2007;40(14):3169-77.

38. Anssari-Benam A. Structure-Function Relationships in the Aortic Valve. London: University of London; 2012.

39. Bashey RI, Torii S, Angrist A. Age-related collagen and elastin content of human heart valves. J Gerontol. 1967 Apr;22(2):203-8.

40. Scott MJ, Vesely I. Morphology of porcine aortic valve cusp elastin. J Heart Valve Dis. 1996 Sep;5(5):464-71.

41. Vesely I. The role of elastin in aortic valve mechanics. J Biomech. 1998 Feb;31(2):115-23.

42. Vesely I, Shi Y, Dobkin D, Iyer R, Soundararajan A, editors. Progress in Developing a Composite Tissue-Engineered Aortic Valve. Engineering in Medicine and Biology Society, 2005 IEEE-EMBS 2005 27th Annual International Conference of the; 2005 17-18 Jan. 2006.

43. Tseng H, Grande-Allen KJ. Elastic fibers in the aortic valve spongiosa: A fresh perspective on its structure and role in overall tissue function. Acta Biomaterialia. 2011;7(5):2101-8.

44. Chandran KB. Role of Computational Simulations in Heart Valve Dynamics and Design of Valvular Prostheses. Cardiovasc Eng Technol. 2010 Mar;1(1):18-38.

45. Haj-Ali R, Dasi LP, Kim HS, Choi J, Leo HW, Yoganathan AP. Structural simulations of prosthetic tri-leaflet aortic heart valves. J Biomech. 2008;41(7):1510-9.

46. Mohammadi H, Bahramian F, Wan W. Advanced modeling strategy for the analysis of heart valve leaflet tissue mechanics using high-order finite element method. Med Eng Phys. 2009 Nov;31(9):1110-7.

47. Gould PL, Cataloglu A, Clark RE. Mathematical modelling of human aortic valve leaflets. Applied Mathematical Modelling. 1976;1(1):33-6.

48. Gould PL, Cataloglu A, Dhatt G, Chattopadhyay A, Clark RE. Stress analysis of the human aortic valve. Computers & Structures. 1973;3(2):377-84.

49. Li J, Luo XY, Kuang ZB. A nonlinear anisotropic model for porcine aortic heart valves. J Biomech. 2001 Oct;34(10):1279-89.

50. Carmody CJ, Burriesci G, Howard IC, Patterson EA. An approach to the simulation of fluid-structure interaction in the aortic valve. J Biomech. 2006;39(1):158-69.

51. Black MM, Howard IC, Huang X, Patterson EA. A three-dimensional analysis of a bioprosthetic heart valve. Journal of Biomechanics. 1991;24(9):793-801.

52. Marom G, Peleg M, Halevi R, Rosenfeld M, Raanani E, Hamdan A, et al. Fluid-structure interaction model of aortic valve with porcine-specific collagen fiber alignment in the cusps. J Biomech Eng. 2013 Oct 1;135(10):101001-6.

53. Hammer PE, Sacks MS, del Nido PJ, Howe RD. Mass-spring model for simulation of heart valve tissue mechanical behavior. Ann Biomed Eng. 2011 Jun;39(6):1668-79.

54. Stephen C. Cowin SBD. Tissue Mechanics. New York: Springer Science; 2007.

55. Mavrilas D, Missirlis Y. An approach to the optimization of preparation of bioprosthetic heart valves. J Biomech. 1991;24(5):331-9.

56. Fung YC. Biomechanics: Mechanics of Living Tissues. 2nd ed. New York: Springer Science; 1993.

57. Doehring TC, Freed AD, Carew EO, Vesely I. Fractional order viscoelasticity of the aortic valve cusp: an alternative to quasilinear viscoelasticity. J Biomech Eng. 2005 Aug;127(4):700-8.

58. Nekouzadeh A, Pryse KM, Elson EL, Genin GM. A simplified approach to quasi-linear viscoelastic modeling. J Biomech. 2007;40(14):3070-8.

59. Doehring TC, Kahelin M, Vesely I. Mesostructures of the aortic valve. J Heart Valve Dis. 2005 Sep;14(5):679-86.

60. Driessen NJ, Boerboom RA, Huyghe JM, Bouten CV, Baaijens FP. Computational analyses of mechanically induced collagen fiber remodeling in the aortic heart valve. J Biomech Eng. 2003 Aug;125(4):549-57.

61. Hepworth DG, Steven-fountain A, Bruce DM, Vincent JF. Affine versus non-affine deformation in soft biological tissues, measured by the reorientation and stretching of collagen fibres through the thickness of compressed porcine skin. J Biomech. 2001 Mar;34(3):341-6.

62. Hilbert SL, Ferrans VJ, Swanson WM. Optical methods for the nondestructive evaluation of collagen morphology in bioprosthetic heart valves. J Biomed Mater Res. 1986 Nov-Dec;20(9):1411-21.

63. Provenzano PP, Vanderby Jr R. Collagen fibril morphology and organization: Implications for force transmission in ligament and tendon. Matrix Biology. 2006;25(2):71-84.

64. Ourselin Sb, Rueckert D, Smith N, Hammer P, Pacak C, Howe R, et al. Collagen Bundle Orientation Explains Aortic Valve Leaflet Coaptation. Functional Imaging and Modeling of the Heart: Springer Berlin Heidelberg; 2013. p. 409-15.

65. Peskin CS, McQueen DM. Mechanical equilibrium determines the fractal fiber architecture of aortic heart valve leaflets. Am J Physiol. 1994 Jan;266(1 Pt 2):H319-28.

66. Sauren AAHJ. The mechanical behavior of the aortic valve. Eindhoven: Eindhoven University of Technology; 1981.

67. Driessen NJ, Bouten CV, Baaijens FP. Improved prediction of the collagen fiber architecture in the aortic heart valve. J Biomech Eng. 2005 Apr;127(2):329-36.

68. Thubrikar MJ, Nolan SP, Aouad J, Deck JD. Stress sharing between the sinus and leaflets of canine aortic valve. Ann Thorac Surg. 1986 Oct;42(4):434-40.

69. Kas'yanov VA, Purinya BA, Ose VP. Structure and mechanical properties of the human aortic valve. Mechanics of Composite Materials. 1985;20(5):637-47.

70. Shen ZL, Dodge MR, Kahn H, Ballarini R, Eppell SJ. Stress-strain experiments on individual collagen fibrils. Biophys J. 2008 Oct;95(8):3956-63.

71. PixeLINK. 3030 Conroy Road Ottawa OKGC.

72. LabJack Corporation. Lakewood CU.

73. Ability Systems Corporation. 1422 Arnold Avenue Roslyn P.

74. Doehring TC, Kahelin M, Vesely I. Direct measurement of nonuniform large deformations in soft tissues during uniaxial extension. J Biomech Eng. 2009 Jun;131(6):061001.

75. Rock CA, Han L, Doehring TC. Complex Collagen Fiber and Membrane Morphologies of the Whole Porcine Aortic Valve. PLoS ONE. 2014;9(1):e86087.

76. Labrosse MR, Lobo K, Beller CJ. Structural analysis of the natural aortic valve in dynamics: from unpressurized to physiologically loaded. J Biomech. Jul 20;43(10):1916-22.

77. Missirlis YF, Armeniades CD. Stress analysis of the aortic valve during diastole: important parameters. J Biomech. 1976;9(7):477-80.

78. Weston MW, LaBorde DV, Yoganathan AP. Estimation of the shear stress on the surface of an aortic valve leaflet. Ann Biomed Eng. 1999 Jul-Aug;27(4):572-9.

79. Anssari-Benam A, Bader DL, Screen HR. Anisotropic time-dependant behaviour of the aortic valve. J Mech Behav Biomed Mater. 2011 Nov;4(8):1603-10.

80. Billiar KL, Sacks MS. Biaxial mechanical properties of the native and glutaraldehyde-treated aortic valve cusp: Part II--A structural constitutive model. J Biomech Eng. 2000 Aug;122(4):327-35.

81. Cataloglu A, Clark RE, Gould PL. Stress analysis of aortic valve leaflets with smoothed geometrical data. J Biomech. 1977;10(3):153-8.

82. Koch TM, Reddy BD, Zilla P, Franz T. Aortic valve leaflet mechanical properties facilitate diastolic valve function. Comput Methods Biomech Biomed Engin. 2010;13(2):225-34.

83. Ragaert K, De Somer F, Somers P, De Baere I, Cardon L, Degrieck J. Flexural mechanical properties of porcine aortic heart valve leaflets. J Mech Behav Biomed Mater. 2012 Sep;13:78-84.

84. Carew EO, Garg A, Barber JE, Vesely I. Stress relaxation preconditioning of porcine aortic valves. Ann Biomed Eng. 2004 Apr;32(4):563-72.

85. Quinn KP, Winkelstein BA. Preconditioning is correlated with altered collagen fiber alignment in ligament. J Biomech Eng. 2011 Jun;133(6):064506.

86. Doehring TC, Carew EO, Vesely I. The effect of strain rate on the viscoelastic response of aortic valve tissue: a direct-fit approach. Ann Biomed Eng. 2004 Feb;32(2):223-32.

87. Xu B, Chow M-J, Zhang Y. Experimental and modeling study of collagen scaffolds with the effects of crosslinking and fiber alignment. International journal of biomaterials. 2011;2011:172389-12.

88. De Hart J, Peters GW, Schreurs PJ, Baaijens FP. Collagen fibers reduce stresses and stabilize motion of aortic valve leaflets during systole. J Biomech. 2004 Mar;37(3):303-11.

89. Legerlotz K, Riley GP, Screen HRC. Specimen dimensions influence the measurement of material properties in tendon fascicles. Journal of Biomechanics. 2010;43(12):2274-80.

90. Anssari-Benam A. Is the time-dependent behaviour of the aortic valve intrinsically quasi-linear? Mechanics of Time-Dependent Materials. 2014;18(2):339-48.

91. Shen ZhileiÂ L, Kahn H, Ballarini R, Eppell StevenÂ J. Viscoelastic Properties of Isolated Collagen Fibrils. Biophysical Journal. 2011;100(12):3008-15.

92. Balachandran K, Sucosky P, Jo H, Yoganathan AP. Elevated cyclic stretch alters matrix remodeling in aortic valve cusps: implications for degenerative aortic valve disease. Am J Physiol Heart Circ Physiol. 2009 Mar;296(3):H756-64.

93. Weiler M, Yap CH, Balachandran K, Padala M, Yoganathan AP. Regional analysis of dynamic deformation characteristics of native aortic valve leaflets. J Biomech. 2011 May 17;44(8):1459-65.

94. Grande KJ, Kunzelman KS, Cochran RP, David TE, Verrier ED. Porcine aortic leaflet arrangement may contribute to clinical xenograft failure. ASAIO J. 1993 Oct-Dec;39(4):918-22.

95. Komolafe OA. Fascicle Scale Experimental and Computational Analysis of the Achilles' Tendon. Philadelphia, PA: Drexel University; 2010.

Appendix Supplementary Figures

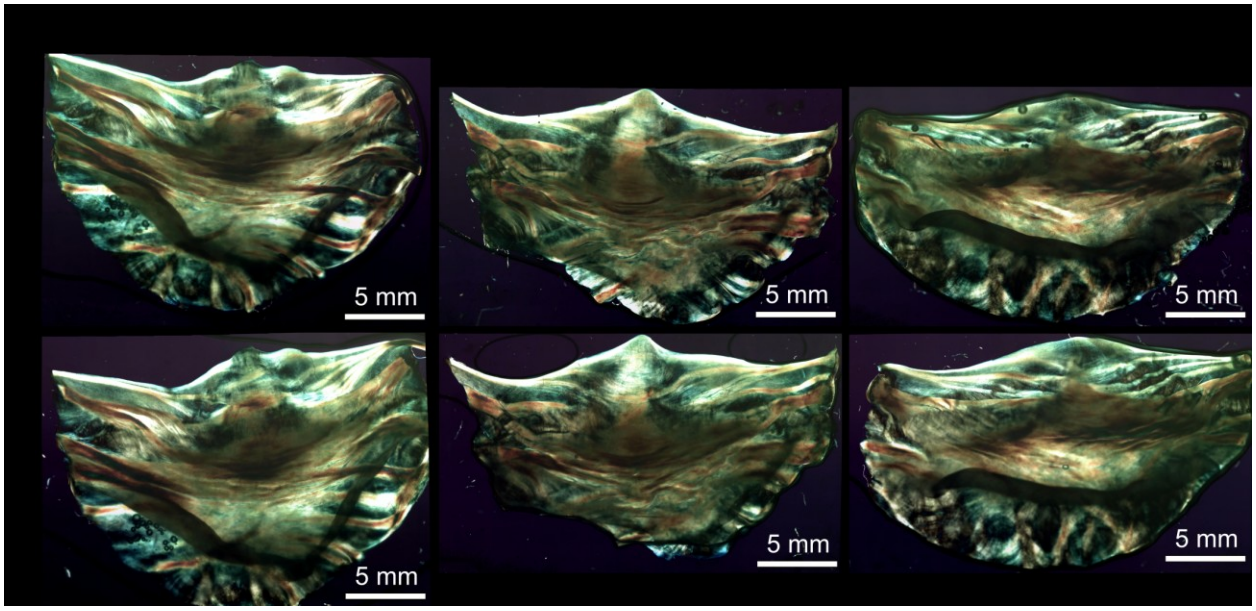

Figure 35 Polarized light images of aortic leaflets with different layers on top. All leaflets from this image came from the same heart. The ventricularis layer images are flipped vertically to ease comparison. We observed only marginal differences in the images.

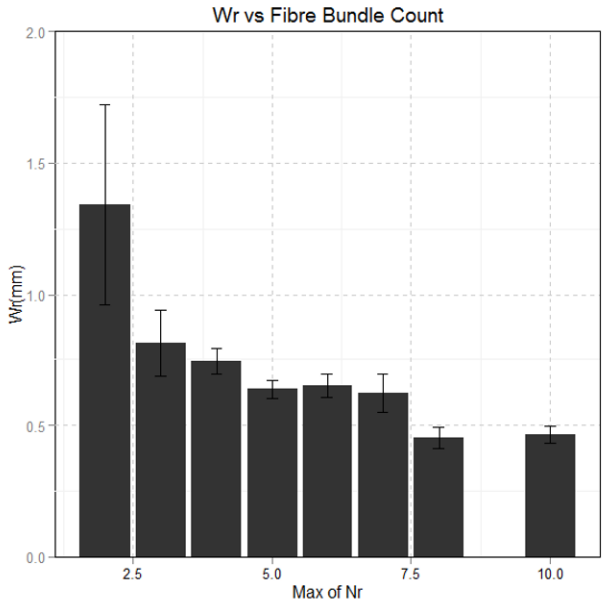

Figure 36 Bar graph of fiber bundle root width W_r as a function of number of fiber bundles (max of N_r). As the number of fiber bundles increase, the mean width decreases.

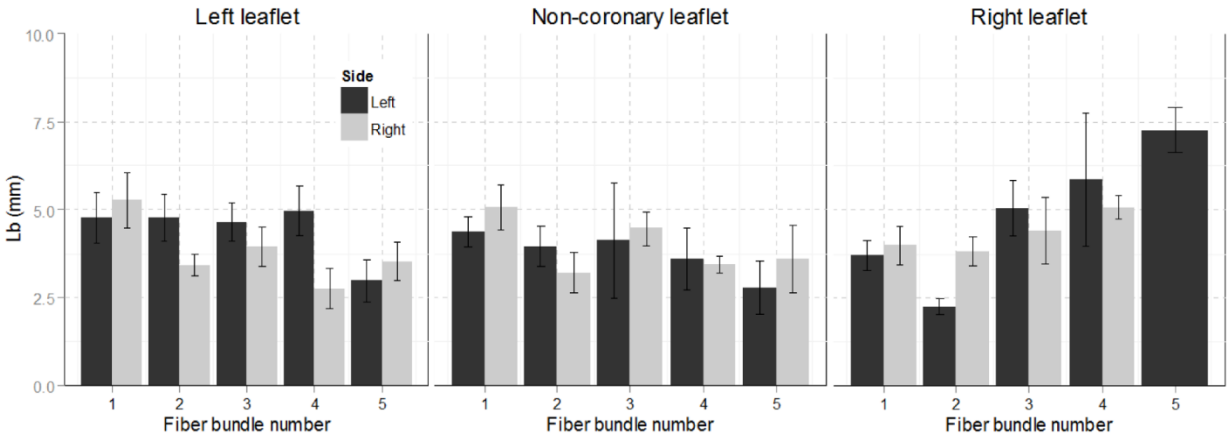

Figure 37 Bar graphs of the length to the first branch point (L_b) for the for fiber bundles on the left and right sides of each leaflet relative to their position from the free edge (N_r). Error bars indicate standard error. While there is no significant difference in the mean distance from leaflet to leaflet or from side to side, the right coronary leaflet's lower fiber bundles branched at a greater distance from the root than the bundles closer to the free edge. ANOVA1: Leaflet = .9637, Side = .31, $N_r = 2.6026*10^{-11}$.

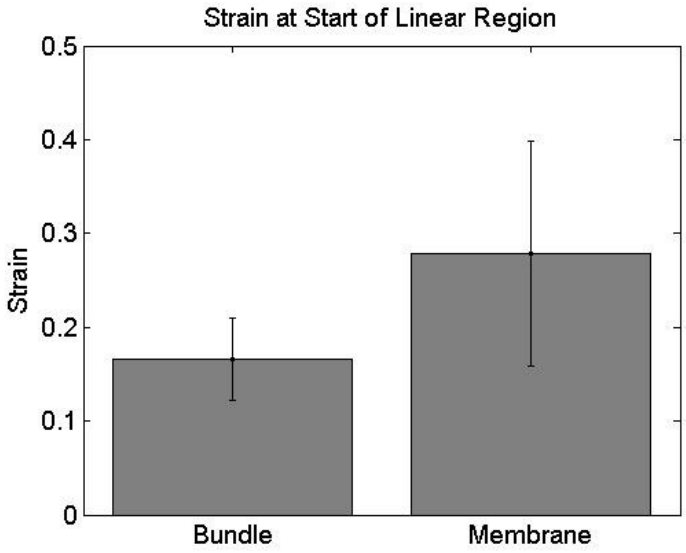

Figure 38 Bar graph of the strain at the start of the linear region for fiber bundle and membrane specimens. Strain has been normalized to 0 at the start of loading. Error bar indicates standard error. T-test shows no significant difference between the fiber bundle and membrane specimens (p >0.05).

Vita

Christopher A Rock

Education

Drexel University, Philadelphia, PA **2006-2015**

Ph.D., Biomedical Engineering (estimated completion September 2015)

Rutgers University, New Brunswick, NJ **2002-2006**

B.S., Biomedical Engineering

Research Experience

Drexel University, Philadelphia, PA **Ph.D. Thesis**

Polarized light microscopy, mechanical testing system design and construction, signal processing, soft tissue mechanical testing, optical strain tracking, non-linear elastic and viscoelastic mathematical modeling.

Rutgers University, New Brunswick, NJ **Undergrad Thesis**

Neural network modeling of Alzheimer's disease.

Publications/Conference Papers

Rock CA, Han L, Doehring TC. Complex collagen fiber and membrane morphologies of the whole porcine aortic valve. PLoS One. 2014 Jan 21;9(1):e86087. doi: 10.1371/journal.pone.0086087. http://www.ncbi.nlm.nih.gov/pmc/articles/PMC3897645/

(Under Review) Rock CA, Han L, Doehring TC. Biomechanical Properties of Fiber Bundle and Membrane Mesostructures of the Porcine Aortic Valve. The Journal of Heart Valve Disease

Rock CA, Doehring T. Mechanics of Aortic Valve Leaflet Mesostructures. Bioengineering Conference (NEBEC), 2012 38th Annual Northeast; 01/2012

Rock CA, Doehring TC. Mesostructure-scale testing system: Electrospun scaffolds. Bioengineering Conference (NEBEC), 2011 IEEE 37th Annual Northeast; 01/2011

Work Experience

Teaching Assistant for Drexel School of Bioscience & Biotechnology **2007-2015**